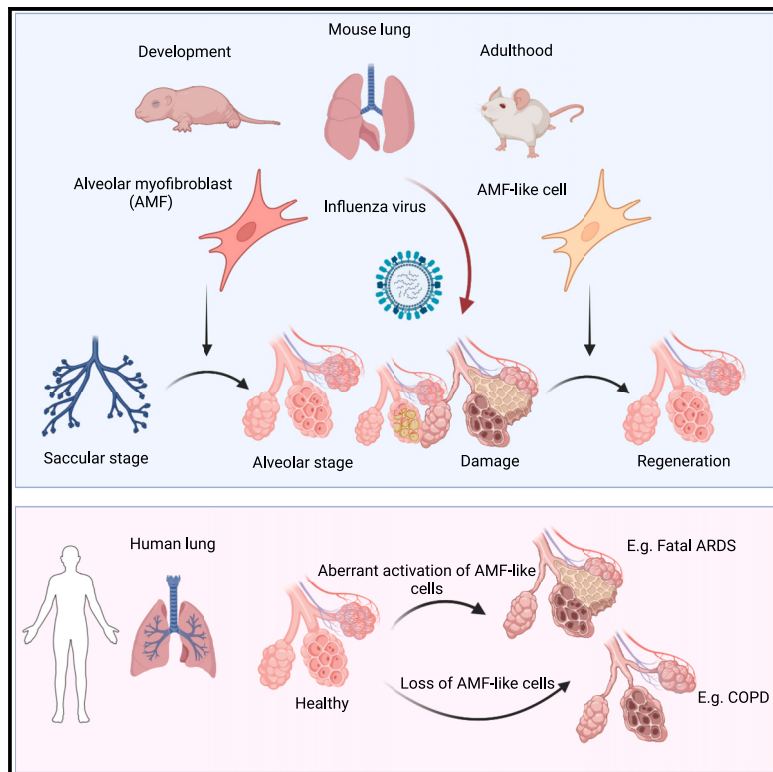


Myofibroblasts emerge during alveolar regeneration following influenza-virus-induced lung injury

Graphical abstract



Authors

Ali Khadim, Georgios Kiliaris,
Ana Ivonne Vazquez-Armendariz, ...,
Rory E. Morty, Susanne Herold,
Elie El Agha

Correspondence

elie.el-agha@innere.med.uni-giessen.de

In brief

Khadim et al. use mouse models to show that adult lung mesenchymal cells upregulate the developmental alveolar myofibroblast (AMF) signature during alveolar regeneration. They show that overactivation or loss of AMF-like cells is observed in humans with fatal acute respiratory distress syndrome (ARDS) or chronic obstructive pulmonary disease (COPD), respectively.

Highlights

- Single-cell RNA-seq identifies alveolar myofibroblasts (AMFs) in alveogenesis
- AMF-like cells emerge during regeneration following influenza virus infection
- AMF-like cells genetically resemble fibrosis-associated myofibroblasts (FAMs)
- Dysregulation of AMF-like cells is associated with failed alveolar regeneration



Article

Myofibroblasts emerge during alveolar regeneration following influenza-virus-induced lung injury

Ali Khadim,^{1,2,3} Georgios Kiliaris,^{1,2,3} Ana Ivonne Vazquez-Armendariz,^{1,2,3,4} Tara Procida-Kowalski,^{2,3,5} David Glaser,^{2,3,5} Marek Bartkuhn,^{2,3,5} Tanya Malik,^{1,2,3} Xuran Chu,^{2,3,6,7,8} Alena Moiseenko,⁹ Irina Kuznetsova,^{1,2,3} Negah Ahmadvand,¹⁰ Arun Lingampally,^{1,2,3,6} Stefan Hadzic,^{2,3,6} Ioannis Alexopoulos,^{1,2,3} Yuexin Chen,^{11,12} Andreas Günther,^{2,3,6} Jürgen Behr,¹² Jens Neumann,¹³ Herbert B. Schiller,^{11,12} Xiaokun Li,^{7,8} Norbert Weissmann,^{2,3,6} Thomas Braun,¹⁴ Werner Seeger,^{2,3,6,14} Małgorzata Wygrecka,^{2,3,6} Rory E. Morty,¹⁵ Susanne Herold,^{1,2,3} and Elie El Agha^{1,2,3,7,16,*}

¹Department of Medicine V, Internal Medicine, Infectious Diseases and Infection Control, Universities of Giessen and Marburg Lung Center (UGMLC), German Center for Lung Research (DZL), Justus Liebig University Giessen, 35392 Giessen, Germany

²Cardio-Pulmonary Institute (CPI), 35392 Giessen, Germany

³Institute for Lung Health (ILH), 35392 Giessen, Germany

⁴University of Bonn, Transdisciplinary Research Area Life and Health, Organoid Biology, Life & Medical Sciences Institute, 53115 Bonn, Germany

⁵Biomedical Informatics and Systems Medicine, Justus-Liebig-University Giessen, 35392 Giessen, Germany

⁶Department of Medicine II, Internal Medicine, Pulmonary and Critical Care, Universities of Giessen and Marburg Lung Center (UGMLC), German Center for Lung Research (DZL), Justus Liebig University Giessen, 35392 Giessen, Germany

⁷Oujiang Laboratory (Zhejiang Lab for Regenerative Medicine, Vision and Brain Health), School of Pharmaceutical Science, Wenzhou Medical University, Wenzhou, Zhejiang 325035, China

⁸School of Pharmaceutical Sciences, Wenzhou Medical University, Wenzhou, Zhejiang 325035, China

⁹Immunology and Respiratory Department, Boehringer Ingelheim Pharma GmbH, Biberach 88400, Germany

¹⁰Department of Cell Biology, Duke University School of Medicine, Durham, NC 27710, USA

¹¹Research Unit Precision Regenerative Medicine (PRM), Comprehensive Pneumology Center (CPC), German Center for Lung Research (DZL), 81377 Munich, Germany

¹²Institute of Experimental Pneumology, LMU University Hospital, Ludwig-Maximilians University, 80336 Munich, Germany

¹³Department of Medicine V, LMU University Hospital, LMU Munich, Comprehensive Pneumology Center, German Center for Lung Research (DZL), 80336 Munich, Germany

¹⁴Max Planck Institute for Heart and Lung Research, W.G. Kerckhoff Institute, 61231 Bad Nauheim, Germany

¹⁵Department of Translational Pulmonology, Heidelberg University Hospital, 69117 Heidelberg, Germany

¹⁶Lead contact

*Correspondence: elie.el-agha@innere.med.uni-giessen.de

<https://doi.org/10.1016/j.celrep.2025.115248>

SUMMARY

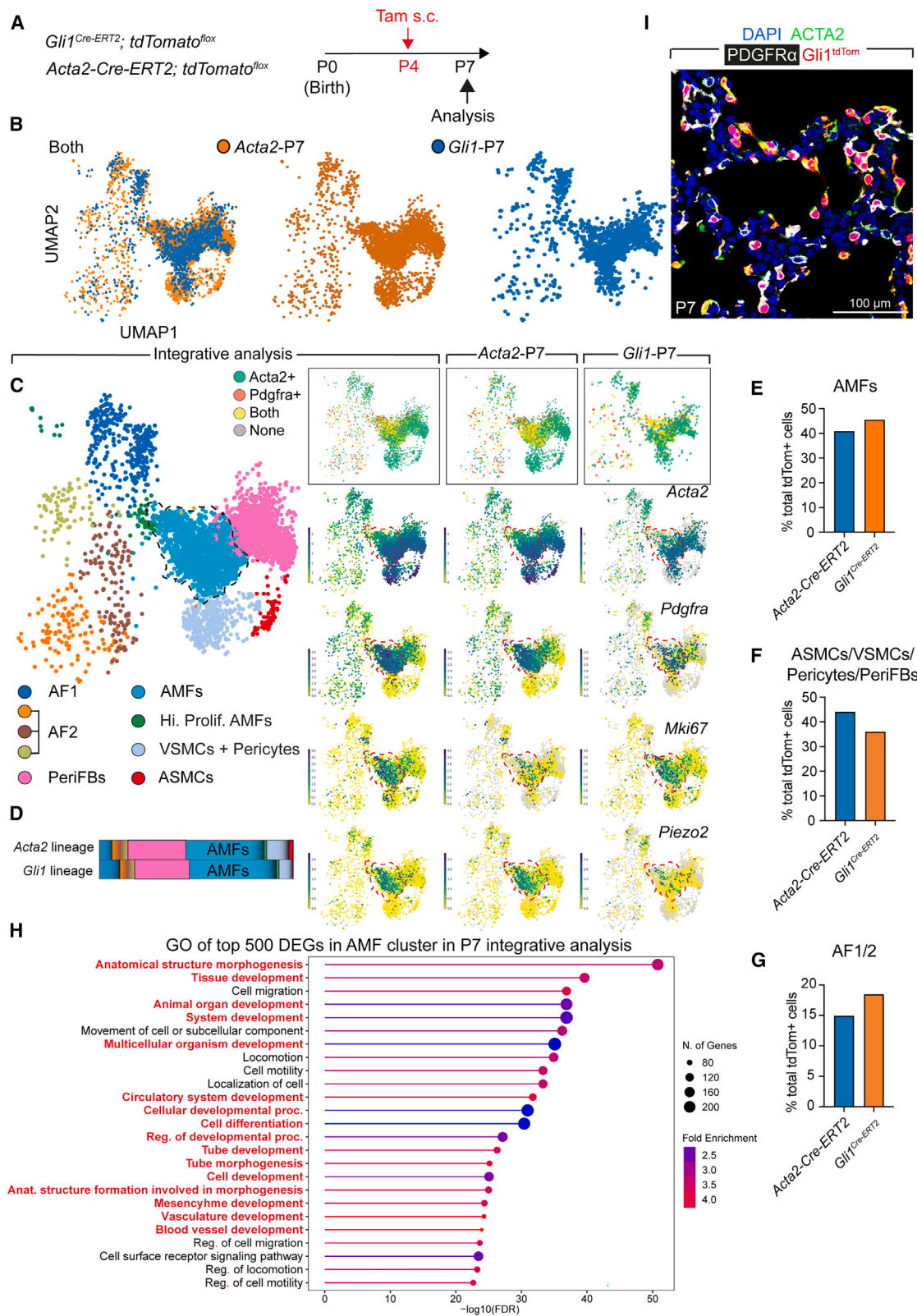
Alveolar regeneration requires the coordinated engagement of epithelial stem cells and mesenchymal niche cells to restore the intricate alveolar architecture of the lung. The current paradigm is that certain aspects of lung organogenesis are mimicked during injury repair in the adult stage. Here, we employ a longitudinal single-cell transcriptomic survey to fate map lung mesenchymal cells throughout development and adulthood. We show that myofibroblasts that are reminiscent of developmental alveolar myofibroblasts (AMFs), termed AMF-like cells, are activated during alveolar regeneration following influenza-virus-induced lung injury. Although AMF-like cells share a similar transcriptomic signature with myofibroblasts that are associated with aberrant repair and fibrosis, these cells do not derive from fibroblast growth factor 10-positive alveolar fibroblasts, and their dysregulation is associated with failed alveolar regeneration in humans. Our data emphasize the role played by developmental mechanisms in alveolar regeneration and highlight the context-dependent nature of myofibroblast biology and function during injury repair.

INTRODUCTION

Lung development concludes with the alveolar stage, where primitive alveolar sacs are subdivided into the smallest respiratory units of the lung, the alveoli. During developmental alveologenesis, a mesenchymal cell population emerges that shares common characteristics with fibroblasts and smooth muscle cells (SMCs) and is commonly referred to as secondary crest

myofibroblasts (SCMFs) or simply alveolar myofibroblasts (AMFs).^{1–4} AMFs express alpha smooth muscle actin (*Acta2*), platelet-derived growth factor receptor alpha (*Pdgfra*), and glioma-associated oncogene homolog 1 (*Gli1*) and are believed to promote alveologenesis.^{5–18} Signaling pathways such as insulin-like growth factor (IGF), WNT, and sonic hedgehog have been implicated in AMF formation.^{18–20} To date, it is widely believed that after developmental alveologenesis is fulfilled, AMFs are





(legend on next page)

eliminated from the lung via apoptotic clearance.^{21,22} There are some lines of evidence implying that AMF-like cells and/or the accompanying developmental mechanisms might be involved in alveolar repair and regeneration during adult life. For example, it was previously shown that the engraftment of neonatal ACTA2+ fibroblasts in elastase-challenged adult mouse lungs (intratracheal instillation of elastase leads to a severe form of alveolar destruction and emphysema) improves alveolar repair.²³ More recently, it was shown that mesenchymal cell contraction is critical not only for alveolar septation during lung development but also for compensatory lung growth following unilateral partial pneumonectomy (PNX) in adult mice, although such findings were not directly attributed to AMFs or AMF-like cells.²⁴ These data support the notion that AMF-associated developmental events might be mimicked during alveolar regeneration in the injured adult lung.

On the other hand, acute respiratory distress syndrome (ARDS) represents a serious health threat worldwide. The mortality rate for patients with ARDS is around 40%, and current treatment is mainly supportive in the absence of strategies and therapeutic agents that can promote alveolar regeneration. While basic research has identified multiple populations of epithelial progenitor and stem cells that are responsible for the repair process, such as subsets of airway and alveolar epithelial cells and their transitional states,^{25–30} little is known about the mesenchymal niche that hosts these cells within the lung tissue and influences their behavior during injury and regeneration. We have previously shown that resident mesenchymal cells assist alveolar regeneration by producing fibroblast growth factor 10 (FGF10), which acts on epithelial progenitors to promote repair following influenza A virus (IAV) infection.³¹ FGF7 derived from mesenchymal alveolar niche cells (MANCs) is also important for alveolar repair following IAV infection.³² The critical role played by mesenchymal cells in the context of pneumonia-induced ARDS was further emphasized with the identification of damage-responsive fibroblasts (DRFibs) that produce the extracellular matrix (ECM) protease ADAMTS4 and drive lethal immunopathology.³³ In this study, we investigated whether AMF-like cells are involved in lung regrowth and regeneration. Using lineage tracing, single-cell transcriptomics, three-dimensional (3D) confocal imaging, and *ex vivo* organoid assays, we show that AMF-like cells emerge during alveolar regeneration. Our data demonstrate that developmental mechanisms are mimicked to restore lung homeostasis following viral pneumonia and that their persistent activation or loss is associated with non-

resolving human lethal ARDS or chronic obstructive pulmonary disease (COPD), respectively.

RESULTS

Characterization of AMFs and their fate during developmental alveologenesis and adulthood

To characterize AMFs, two independent genetic approaches were employed: *Acta2-Cre-ERT2*; *tdTomato*^{flx} to label ACTA2+ cells and *Gli1-Cre-ERT2*; *tdTomato*^{flx} to label GLI1+ cells (Figure S1). Cells were labeled by a single subcutaneous (s.c.) injection of tamoxifen at post-natal day (P)4, a time point that precedes alveolarization that starts at P5, and lungs were harvested at various time points corresponding to developmental alveologenesis (P7 and P14) and maturation (P28), adulthood (P56), and beyond (P182) (Figures S1A and S1J). Histological analysis of thick sections revealed a high abundance of parenchymal *Acta2*-traced *tdTom+* at P7 and P14, with a gradual decline through P28 to P182 (Figures S1B–S1F). These cells were mostly ACTA2+ at P7 but not at later time points (Figures S1B–S1D and S1G). As expected, the majority of parenchymal *tdTom+* cells that were initially ACTA2+ were predominantly PDGFR α + (Figures S1E and S1H). Thus, they were identified as AMFs at P7. The *tdTom*-lineage maintained *Pdgfra* expression throughout all analyzed time points (Figures S1E and S1H). Analysis of Ki-67 immunostaining revealed massive proliferation at P7 but not at later time points (Figure S1I). Similar analysis of the GLI1+ cell lineage labeled at P4 and analyzed at various time points also confirmed that the AMFs can be labeled using this experimental approach (Figures S1J–S1R). Like AMFs labeled using the *Acta2-Cre-ERT2*; *tdTomato*^{flx} approach, analysis of GLI1+ cells also showed that these cells are initially ACTA2+ (Figure S1K) and predominantly proliferative at P7 (Figures S1N and S1O) and that both features essentially diminish over the time course of alveolar maturation, adulthood, and beyond (Figures S1Q and S1R).

To further characterize these cells, a longitudinal single-cell RNA sequencing (scRNA-seq) survey was carried out on *tdTom+* cells that were fluorescence-activated cell sorted from *Acta2-Cre-ERT2*; *tdTomato*^{flx} or *Gli1-Cre-ERT2*; *tdTomato*^{flx} lungs (Figure S2). Fluorescence-activated cell sorting (FACS) analysis confirmed the decline in cell abundance over time (Figures S2B and S2K), thus agreeing with histological quantifications (Figures S1F and S1P), and ACTA2+ PDGFR α + cells were detected at P7 (Figures S2D, S2F, and S2M). Other cellular clusters included alveolar fibroblasts 1 and 2 (AF1/2s), peribronchial

Figure 1. Identification of the alveolar myofibroblast cluster at P7

(A) Timeline and experimental design. The P7 datasets were extracted from the integrative analysis for all time points shown in Figure S2.

(B) Integrative and single UMAPs at P7.

(C) Integrative UMAP highlighting the AMF cluster at P7 and showing selected markers.

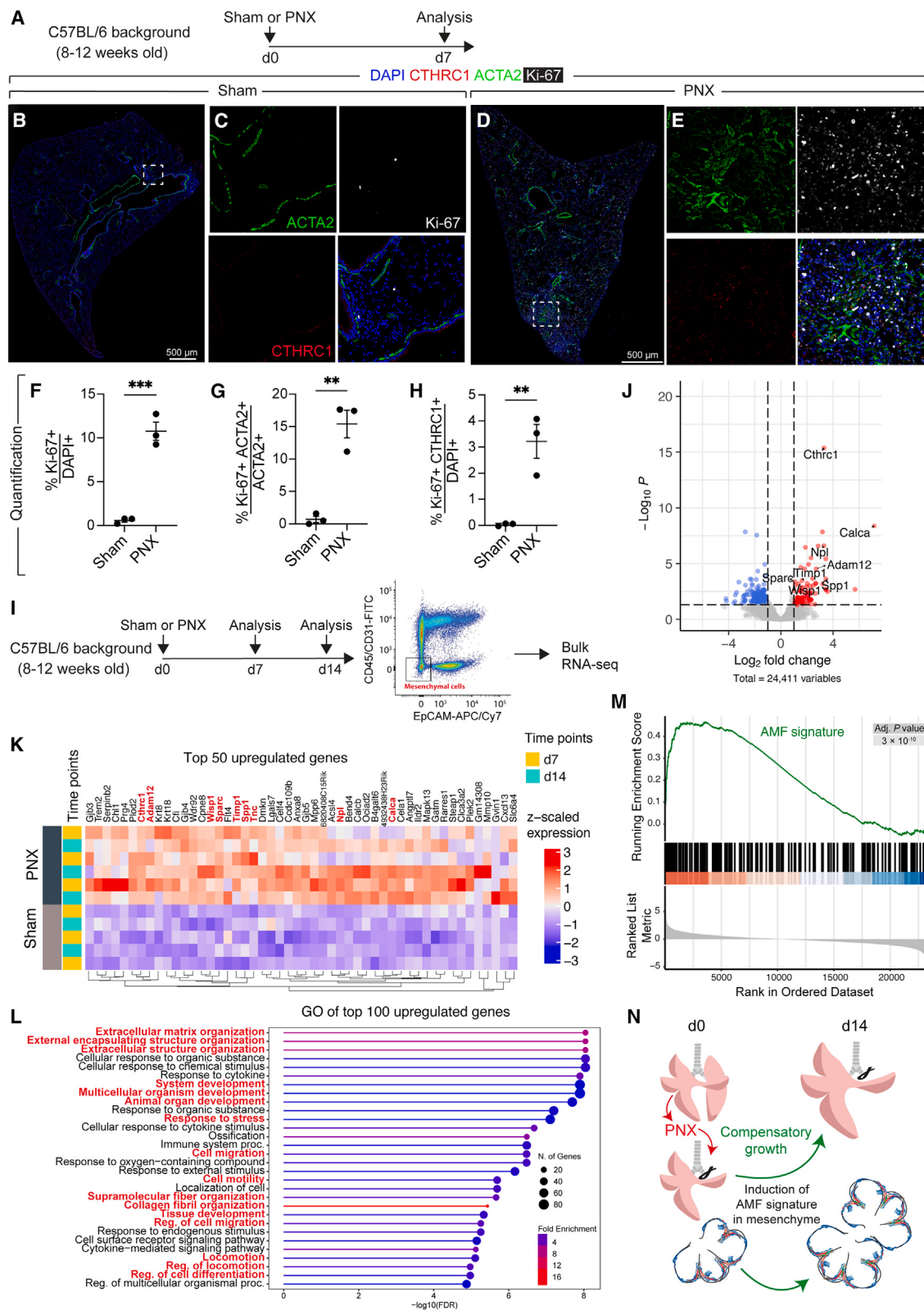
(D–G) Quantification of the AMF cluster as well as other clusters at P7.

(H) Gene Ontology (GO) analysis of the top 500 differentially regulated genes (DEGs) in the AMF cluster.

(I) Immunofluorescence using indicated antibodies.

AF1, alveolar fibroblasts 1; AF2, alveolar fibroblasts 2/matrix fibroblasts 2/adventitial fibroblasts; AMFs, alveolar myofibroblasts; ASMCs, airway smooth muscle cells; Hi. Prolif. AMFs, highly proliferative AMFs; PeriFBs, peribronchial fibroblasts; VSMCs, vascular smooth muscle cells. $n = 3$ animals per group. Scale bar: 100 μ m. (C) For the integrative analysis of the *Acta2-Cre-ERT2*; *tdTomato*^{flx} and *Gli1-Cre-ERT2*; *tdTomato*^{flx} datasets, the initial numbers of cells sequenced were 2,813 and 1,474, respectively. After removal of contaminants, 2,799 and 1,462 cells were used for the analysis. Clusters 6, 7, 16, 18, 19, and 20 (Leiden 1.0) were identified as contaminants and therefore removed.

See also Figures S2–S6 and Data S1.



(legend on next page)

fibroblasts (PeriFBs), and SMCs (Figures S2C, S2G, S2H, and S2L–S2P). We also verified that analyzed cells express *Wpre* (tdTom) (Figures S3A and S3B) but not epithelial or endothelial markers (Figure S3C). Interestingly, *Acta2*-lineage-traced cells seemed to be more significantly cleared compared to *Gli1*-lineage-traced cells over time (Figures S1F, S1P, S2B, and S2K), indicating that cells responding to hedgehog signaling neonatally represent a more stable cell population and therefore retained more than cells that express *Acta2*. Notably, both datasets showed that the remaining cells were largely AF1/2s at later stages (Figures S2G and S2P), indicating that they may regulate alveolar homeostasis during adulthood and aging. Integrative analysis of the two datasets at P7 identified the AMF cluster defined as ACTA2+ PDGFR α + (Figures 1A–1C and 1I), which accounted for around 40%–45% of total labeled cells at P7 (Figure 1E). The AMF cluster was also the most proliferative compared to other clusters (*Mki67* uniform manifold approximation and projection [UMAP] plot in Figure 1C). Other clusters were identified as airway and vascular SMCs (ASMCs and VSMCs, respectively), pericytes, PeriFBs (Figures 1C and 1F), and, to a lesser extent, AF1/2s (Figures 1C and 1G). Using this P7 time point where AMFs are most abundant, we established a gene signature for these cells (Data S1). Gene Ontology (GO) analysis of the P7 AMF signature (top 500 differentially expressed genes [DEGs]) showed that the top enriched pathways were dominated by processes related to morphogenesis and development, such as anatomical structure morphogenesis, tissue development, tube morphogenesis, animal organ development, mesenchyme development, and others (Figure 1H).

Mesenchymal cells display a transcriptomic signature that closely mimics that of developmental AMFs during lung regrowth following PNX

It is widely believed that certain aspects of lung development are mimicked during regrowth or regeneration of the adult lung. As AMFs are regarded as main drivers of developmental alveologenesis, we sought to determine whether their transcriptomic signature is enriched in mesenchymal cells during compensatory lung growth following unilateral partial PNX (Figure 2). Histological analysis of sham and PNX lungs following surgery showed an emergence of proliferative ACTA2+ CTHRC1+ (myofibroblastic) cells in the lung parenchyma at day 7 in PNX mice (Figures 2A–2H). In another set of animals, lungs were digested, and mesenchymal cells were fluorescence-activated cell sorted

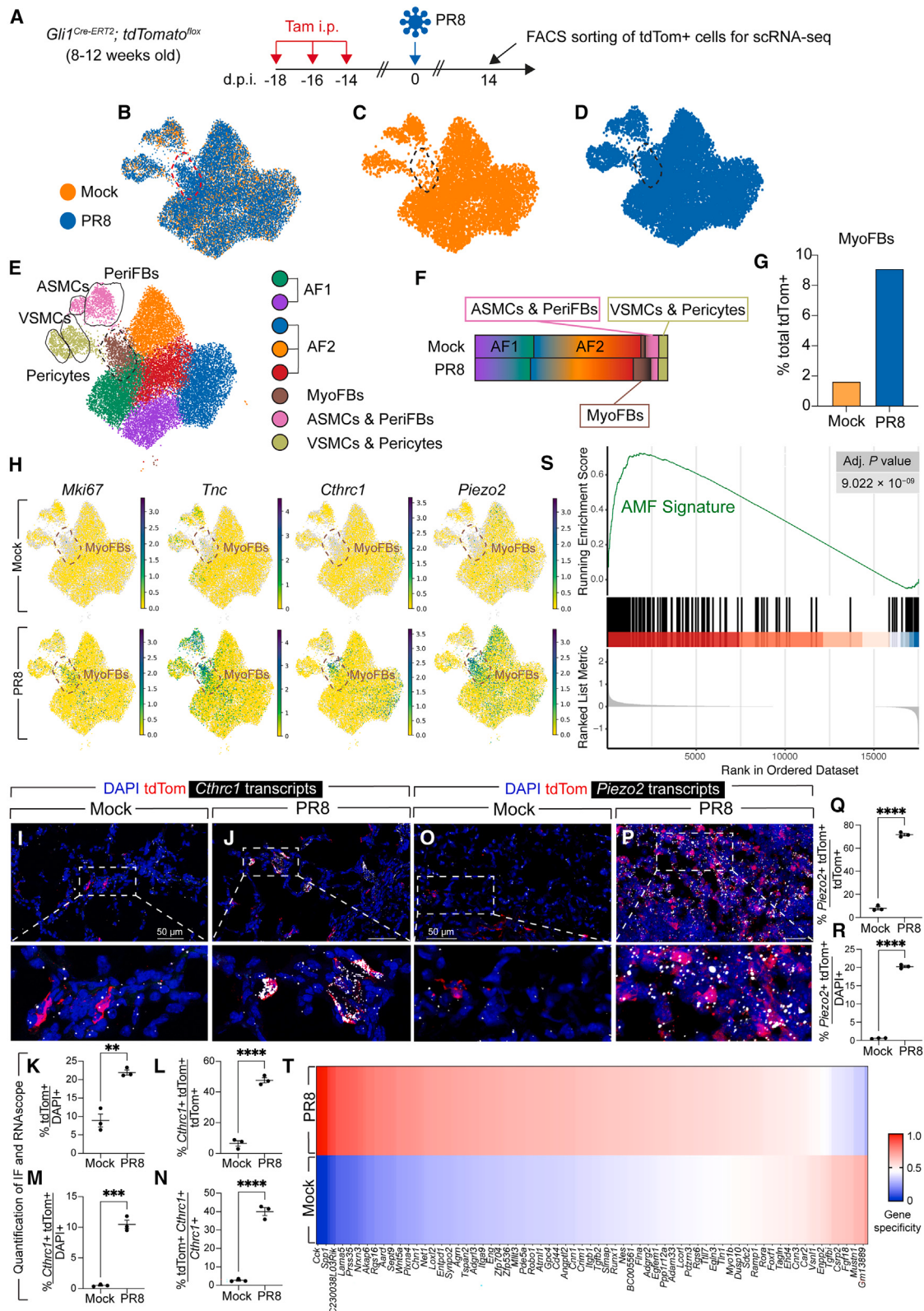
and subjected to bulk RNA-seq (Figure 2I). Myofibroblast (MyoFB) genes were among the top enriched genes in mesenchymal cells isolated from PNX versus sham, including *Cthrc1*, *Calca*, *Npl*, *Adam12*, *Timp1*, *Sparc*, *Spp1*, and *Wisp1* (Figures 2J and 2K). GO analysis showed that such mesenchymal cells were enriched for processes that are related to ECM biology, development, and cell motility, such as ECM organization, structure organization, system development, animal organ development, cell migration, cell motility, supramolecular fiber organization, collagen fibril organization, and others (Figure 2L). Importantly, gene set enrichment analysis (GSEA) revealed that the AMF signature, defined as the top 200 DEGs at P7 (Figure 1; Data S1), was significantly upregulated (adjusted [adj.] $p = 3 \times 10^{-10}$) in mesenchymal cells derived from PNX lungs (Figure 2M). These results show that the developmental AMF signature is enriched in mesenchymal cells during compensatory lung regrowth (Figure 2N). We also investigated the signature of the other developmental P7 clusters and observed significant downregulation for AF1 (adj. $p = 3 \times 10^{-10}$), significant enrichment for PeriFBs (adj. $p = 4.312 \times 10^{-8}$), and weaker enrichment for AF2 (adj. $p = 0.0003136$), ASMCs (adj. $p = 0.0006079$), and VSMCs + pericytes (adj. $p = 0.005663$) in D7 PNX compared to sham (data not shown).

AMF-like cells emerge in response to influenza virus infection

To determine whether AMF-like MyoFBs contribute to alveolar regeneration following influenza-virus-induced lung injury, 8- to 12-week-old *Gli1*^{Cre-ERT2}; *tdTomato*^{flx} mice were treated with tamoxifen before being infected with influenza A/Puerto Rico/8/34 H1N1 (PR8) or mock, and fluorescence-activated cell-sorted tdTom+ cells were subjected to scRNA-seq at day 14, a time point corresponding to active regeneration (Figure 3A). The data showed a clear emergence of MyoFBs in response to PR8 infection (Figures 3B–3G). These cells were enriched for *Mki67* as well as typical MyoFB markers, including *Tnc* and *Cthrc1* (Figure 3H). These cells also expressed *Piezo2* (Figure 3H). To confirm the scRNA-seq data, we carried out RNA-seq for *Cthrc1* and *Piezo2*, and the results revealed, in addition to an increase in the abundance of tdTom+ cells, a striking increase in the expression of *Cthrc1* and *Piezo2* upon infection, particularly in tdTom+ cells (Figures 3I–3R). Interestingly, *Piezo2* showed a wider expression pattern compared to *Cthrc1* where more than 70% of tdTom+ cells expressed *Piezo2*.

Figure 2. Mesenchymal cells upregulate the AMF gene signature after pneumonectomy

- (A) Timeline and experimental design.
 - (B–E) Immunofluorescence using indicated antibodies (B and D). The regions marked with dashed boxes are magnified in (C) and (E).
 - (F–H) Quantification of the immunofluorescence shown in (B)–(E).
 - (I) Timeline and experimental design.
 - (J) Volcano plot showing upregulation of AMF signature genes in PNX versus sham.
 - (K) Heatmap showing the top 50 upregulated genes in PNX versus sham. Selected myofibroblast markers are marked in red font.
 - (L) Gene Ontology (GO) analysis of the top 100 upregulated genes in PNX versus sham. AMF-related pathways are marked by red font.
 - (M) Gene set enrichment analysis (GSEA) showing enrichment of the AMF signature (top 200 DEGs extracted from P7 scRNA-seq dataset in Figure 1 and Data S1) in PNX versus sham.
 - (N) Model showing upregulation of the AMF signature in mesenchymal cells during regeneration following PNX.
- AMF, alveolar myofibroblast; PNX, pneumonectomy. (A–H) $n = 3$ per group and (K–M) sham day 7 $n = 3$, PNX day 7 $n = 3$, sham day 14 $n = 2$, and PNX day 14 $n = 3$. (F–H) Data are represented as mean \pm SEM. ** $p < 0.01$ and *** $p < 0.001$. Scale bars: 500 μ m.
- See also Data S1.



(legend on next page)

(Figure 3Q) and *Piezo2*+ tdTom+ (double-positive) cells represented 20% of total DAPI+ cells in PR8-infected lungs (Figure 3R). Of note, developmental P7 AMFs also expressed *Piezo2* (Figures 1C and S2R). To investigate whether adult GLI1+ cell-derived MyoFBs resemble developmental P7 AMFs, we carried out GSEA for the top 200 DEGs constituting the P7 AMF signature identified in Figure 1 and Data S1 in the MyoFB cluster of mock and PR8-infected samples. The results showed significant upregulation for this signature in the PR8 sample (Figures 3S and 3T). We also carried out enrichment analysis for the remaining P7 clusters, and the data showed significant enrichment for PeriFBs (adj. $p = 1 \times 10^{-10}$) and AF1 (adj. $p = 1.725 \times 10^{-5}$) and weaker or no significant enrichment for ASMCs (adj. $p = 0.007248$), VSMCs + pericytes (adj. $p = 0.07286$), and AF2 (adj. $p = 0.07889$) (data not shown). The scRNA-seq datasets from adult mock and PR8-infected mice were also integrated with the P7 and P28 (both labeled at P4) datasets (Figures S4A and S4B). Integrative analysis showed that the MyoFBs emerging after infection cluster with developmental AMFs (Figures S4C and S4D); thus, we dubbed them AMF-like cells. Similar to AMFs, these cells are proliferative (Figure S4F) and express typical MyoFB markers such as *Acta2* (Figure S4E), *Cthrc1* (Figure S4G), and *Tnc* (Figure S4H). GO analysis of the AMF and AMF-like clusters in PR8-infected mice showed enrichment for proliferative and developmental/morphogenic pathways such as cell division, tissue development, and others (Figure S4I).

To determine if these AMF-like MyoFBs are pathological or regenerative, we first compared their transcriptomic signature to *bona fide* fibrosis-associated MyoFBs (hereafter referred to as FAMs) that are known to drive aberrant repair and remodeling in response to bleomycin injury. We integrated our dataset with the *Col1a1-EGFP* dataset where *Cthrc1* was identified as a marker for such pathological FAMs³⁴ (Figure S5). Strikingly, AMFs and AMF-like cells formed a single cluster with FAMs (Figures S5B–S5E). GO analysis revealed that the top pathways relate to ECM biology and development/morphogenesis, such as tube development, tube morphogenesis, ECM organization, extracellular structure organization, regulation of cell differentiation, tissue morphogenesis, cell morphogenesis, and others (Fig-

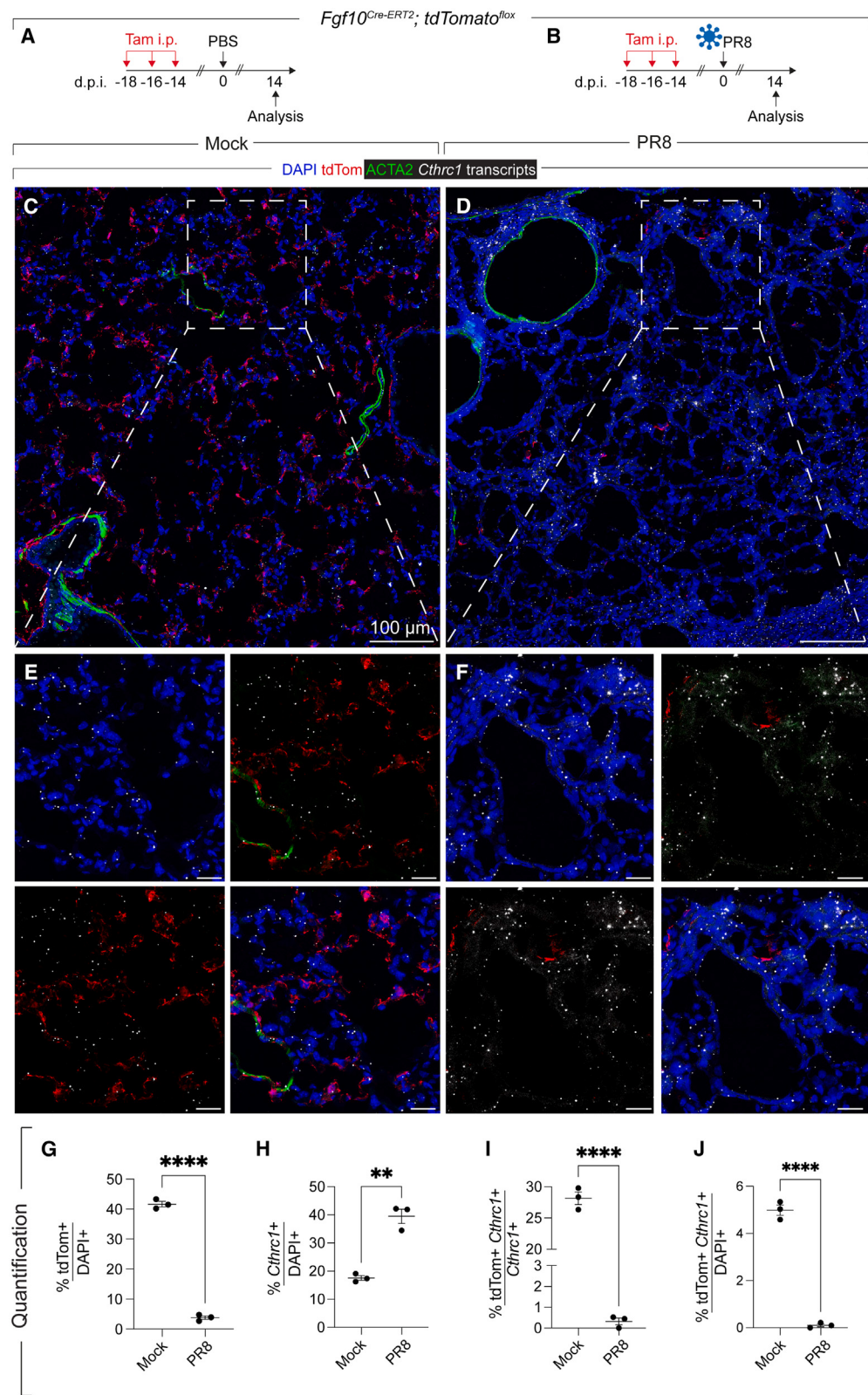
ure S5I). Therefore, we conclude that AMFs and AMF-like cells share a similar transcriptomic signature to pathological FAMs.

We then asked whether AMF-like cells appearing after influenza infection share the same cellular origin as those seen in lung fibrosis. FAMs have been shown to be of mesenchymal origin and feature an important role for the transcription factor TBX4.³⁵ We have shown that FAMs derive from lipofibroblasts, a cell type that belongs to AFs.³⁶ This has also been confirmed by independent investigators.^{37–39} In our previous work, we showed that FGF10+ cells, a population that predominantly includes AFs,^{40–42} contribute to FAMs in the fibrotic lung.³⁶ We therefore employed our recently generated *Fgf10*^{Cre-ERT2} mouse line that allows lineage tracing of AFs in the adult lung⁴¹ as opposed to our previous line, where Cre activity was mostly active during embryonic development.⁴³ Mice were exposed to tamoxifen to label pre-existing FGF10+ cells and infected with PR8 2 weeks after the final tamoxifen injection (Figures 4A and 4B). Histological analysis showed that lineage-labeled cells representing AFs were dramatically lost and were very few during regeneration (Figures 4C–4G). *Cthrc1* expression was, as expected, upregulated in response to PR8 infection (Figures 4C–4F and 4H). While some tdTom+ cells expressed *Cthrc1* at baseline (mock), this expression was dramatically lost after infection (Figures 4C–4F, 4I, and 4J). We also carried out RNAvelocity analysis on the developmental time series as well as the mock and PR8 datasets. Under all experimental conditions, the analysis did not predict differentiation trajectories from FGF10+ AFs to AMFs (during lung development) or AMF-like cells (in PR8-infected adults) (Figures S6A–S6F). On the contrary, the analysis predicted AMF-like-to-AF trajectories in the regenerating lung (Figure S6F). Collectively, these data suggest that unlike pathological FAMs, CTHRC1+ AMF-like cells that appear during regeneration following influenza-virus-induced lung injury do not derive from pre-existing FGF10+ AFs.

We then integrated the *Gli1*^{Cre-ERT2} dataset from P7, P28, (adult) mock, and (adult) PR8 with the single-cell atlas of mouse lung development⁴⁴ and carried out CellChat analysis to reveal cell-cell interactions (Figures 5A–5F). While the P7 AMF cluster revealed strong interactions with AT1s and AT2s (Figure 5C),

Figure 3. Adult GLI1+ cells give rise to myofibroblasts during regeneration following influenza A virus infection

- (A) Timeline and experimental design.
 - (B–D) Integrative and single UMAP plots for mock and PR8-infected samples.
 - (E) Integrative analysis revealing the different cellular clusters within the GLI1+ lineage.
 - (F) Quantification of constituent cellular clusters in each condition.
 - (G) Quantification of myofibroblasts in each condition.
 - (H) UMAP plots for selected proliferation and myofibroblast markers.
 - (I and J) RNAscope for *Cthrc1* counterstained with DAPI.
 - (K–N) Quantification of *Cthrc1* RNAscope.
 - (O and P) RNAscope for *Piezo2* counterstained with DAPI.
 - (Q and R) Quantification of *Piezo2* RNAscope.
 - (S) Gene set enrichment analysis (GSEA) showing highly significant upregulation of the AMF signature (top 200 differentially expressed genes [DEGs] of the AMF cluster extracted from P7 scRNA-seq dataset in Figure 1 and Data S1) in the MyoFB cluster in the PR8 sample compared to mock.
 - (T) Heatmap showing the genes used in (S). Every third gene is shown.
- AF1, alveolar fibroblasts 1; AF2, alveolar fibroblasts 2/matrix fibroblasts 2/adventitial fibroblasts; ASMCs, airway smooth muscle cells; i.p., intraperitoneal injection; MyoFBs, myofibroblasts; PeriFBs, peribronchial fibroblasts; PR8, A/Puerto Rico/8/34 H1N1; VSMCs, vascular smooth muscle cells; Tam, tamoxifen. $n = 3$ animals per group. The initial numbers of cells sequenced for mock and PR8 were 7,630 and 13,675, respectively. Clusters 8, 9, 10, 11, 12, and 13 (Leiden 0.6) were identified as contaminants and therefore removed. The final numbers of cells analyzed for mock and PR8 are 7,264 and 11,828, respectively. (Q, R, and K–N) Data are represented as mean \pm SEM. ** $p < 0.01$, *** $p < 0.001$, and **** $p < 0.0001$. Scale bars: 50 μ m.
- See also Figures S2–S6 and Data S1.



(legend on next page)

these interactions were slightly weaker at P28 (Figure 5D). In the adult stage and in the absence of injury (mock), weaker interactions were observed between the AMF-like cluster and AT1s and AT2s (Figure 5F) while strong interactions were observed after PR8 infection (Figure 5E). These data suggest that AMFs and AMF-like cells strongly interact with AT1s and AT2. The top targets included collagen-syndecan interactions (Figure 5G; Data S1). In line with the bioinformatic prediction, organoid cultures showed that tdTom+ cells isolated from PR8-infected lungs showed superior ability to support AT2 growth *ex vivo* compared to their mock-derived counterparts (Figures 5H–5J). Although the AT2-supportive ability after infection might not be directly attributable to the AMF-like cluster, these data hint at an important *in vivo* role for GLI1+ cells in promoting alveolar regeneration following influenza-virus-induced lung injury *in vivo*.

AMF-like cells are severely reduced in human COPD lungs, and their persistent activation is associated with lethal non-resolving fibrotic ARDS

To investigate the significance of our findings in the human context, we carried out immunofluorescence (IF) on sections from human donor and COPD lung explants. While donor lungs showed baseline levels of CTHRC1 and KI-67 expression in the alveolar regions (Figures 6A–6C and 6E), the expression of these markers was almost completely diminished in the enlarged alveoli of emphysematous COPD lungs (Figures 6B–6D and 6F). Gene expression analysis using lung homogenates from these explanted lungs confirmed the strong downregulation of *GLI1* (Figure 6G) and *CTHRC1* (Figure 6H). Finally, IF on lung sections from autopsies from patients with IAV ARDS revealed a strong expression for ACTA2 and CTHRC1 in heavily remodeled regions of the lung, a pattern that is reminiscent of interstitial lung disease such as idiopathic pulmonary fibrosis (IPF) (Figures 6I–6K). These findings indicate that persistent activation of AMF-like cells in response to IAV-induced pneumonia is likely linked to non-resolving fibrosis in lethal ARDS.

DISCUSSION

There is a consensus that developmental mechanisms are mimicked during repair and regeneration after injury during adult life. This has been proposed in IPF, for instance, where repetitive microinjuries initiate a vicious cycle of injury repair, with morphogenic pathways ultimately being hijacked to drive aberrant remodeling, fibrosis, and respiratory failure. AMFs are a developmental cell type that is prominent during the alveolar stage of lung development. Although these cells transiently populate the lung during developmental alveogenesis, they have regained interest in recent years due to their morphogenic potential and the perspective of exploiting the knowledge gained from

studying these cells to develop novel therapeutic strategies that promote lung regeneration. In this study, we show that mesenchymal cells display an AMF-like signature using mouse models of compensatory lung growth and balanced regeneration of the alveolar network in response to injury and that dysregulation of these cells is associated with impaired regeneration in the human lung.

Compensatory lung growth has been shown to rely on mesenchymal cell contraction, similarly to the events occurring during developmental alveogenesis.²⁴ Although the latter study did not demonstrate an involvement for AMF-like cell contraction in the regenerative process occurring in the adult stage, it is plausible that such effects can be attributed to AMF-like cells. To our knowledge, our study is the first to demonstrate that AMF-like cells are reactivated during lung regeneration. The finding that AMF-like cells emerge in two models of lung regeneration (compensatory regrowth and alveolar regeneration following IAV-induced ARDS) implies that AMFs are likely a key component of the regenerative machinery in the lung.

Factors that reinitiate the developmental program in mesenchymal cells in the adult lung potentially include biophysical forces and stretch such as in the PNX model and/or morphogenic signals that derive from pro-regenerative macrophages, subsets of AT2s, endothelial cells, or other mesenchymal cell subsets. Our bioinformatic predictions revealed strong interactions between neonatal (P7) AMFs and AT1/2s and adult AMF-like cells emerging following influenza-virus-induced lung injury and AT1/AT2s. Previous work has shown that during lung development, AMFs closely interact with AT1 through PDGF, WNT, SHH, and IGF signaling and that perturbation of such pathways impairs alveolarization during post-natal lung development.¹⁸ Another study showed that AMFs can influence AT2 progenitors (termed pAT2s) and their differentiation during development.⁴⁵ Our data reveal that adult AMF-like cells may represent a mesenchymal niche for AT2s after influenza-virus-induced lung injury. Among the top ligand-receptor interactions between AMF-like cells and AT2s are those involving collagen-syndecan interactions. In the future, it will be important to test the effect of perturbations to these interactions on alveolar homeostasis and repair *in vivo* and *ex vivo*.

A recent report has shown that remnants of neonatal ACTA2+ cells that persist in the adult respond to hypoxia or bleomycin injury by re-expressing *Acta2*.⁴⁶ In our work, we applied our neonatal AMF signature in cells labeled in the adult stage, and we demonstrate that such a developmental signature is reactivated during alveolar regeneration. In the future, it will be important to investigate whether the cells originally labeled during the neonatal period are the ones that are reactivated after injury. However, one major drawback is the transgenic mouse lines currently available; these lines obviously label heterogeneous

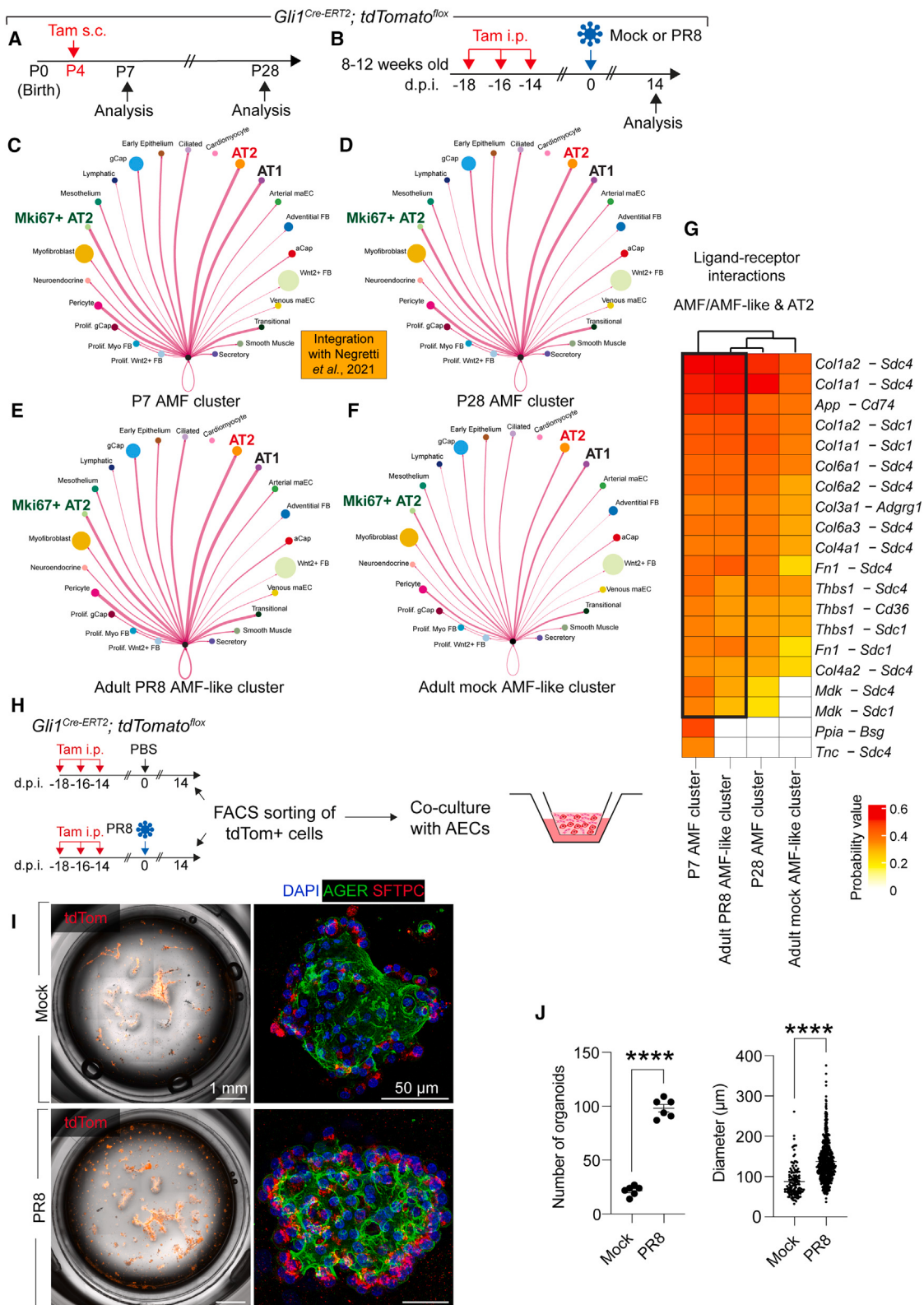
Figure 4. Pre-existing FGF10+ alveolar fibroblasts do not contribute to *Cthrc1*+ AMF-like cells after influenza virus infection

(A and B) Timeline and experimental design.

(C–F) RNAscope for *Cthrc1* and immunofluorescence for ACTA2 counterstained with DAPI in mock and PR8 samples.

(G–J) Quantification of cell populations.

i.p., intraperitoneal injection; PR8, A/Puerto Rico/8/34 H1N1; Tam, tamoxifen. *n* = 3 per group. (G–J) Data are represented as mean ± SEM. ***p* < 0.01 and ****p* < 0.0001. Scale bars: 100 μm.



(legend on next page)

populations of cells, and, to our knowledge, there are no available tools to exclusively target neonatal AMFs. Possibly, such a limitation will be at least partially overcome using intersectional genetics that relies on dual recombinase approaches, such as Cre-ERT2 and Dre-ERT2, to target cellular subsets with more precision based on the expression of two genes instead of one. In addition to lineage tracing and sorting of a pure AMF-like population for organoid assays, it will be important to carry out selective cell ablation *in vivo* to test the requirement of these cells in alveolar regeneration.

We also investigated the enrichment of the other developmental clusters from P7 and found that while GSEA showed significant downregulation for AF1, significant enrichment for PeriFBs, and weaker enrichment for the remaining clusters in the total mesenchyme derived from PNX versus sham, the GLI1+ lineage appeared to globally reinforce its gene signature during alveolar regeneration after PR8 infection, with the most significantly enriched signatures corresponding to AMFs and PeriFBs and the AMF-like cluster uniquely displaying a significant increase in its abundance. The difference in the two observations likely relates to the nature of the analyzed cells (total mesenchyme versus GLI1+ cells) and the different triggers and, therefore, mechanisms of lung injury, repair, and regeneration in the employed models (PNX versus PR8). Future work should address the involvement of non-AMF-like clusters in alveolar regeneration following various models of injury and regeneration. Another intriguing aspect is the strong similarity between AMF-like cells and profibrotic FAMs. Our data revealed that FGF10+ AFs do not give rise to AMF-like cells during lung regeneration in contrast to aberrant repair and fibrosis, where we and others have shown that they are an important source of FAMs.^{36–39} While the latter cells are detrimental to AT2s, AMF-like cells may represent niche cells that promote the growth of AT2s. Whether the cellular origin per se determines if the arising MyoFBs are regenerative (AMF-like) or profibrotic (FAM) requires further investigations. A recent report also identified *Cthrc1* as a marker of transitional fibroblasts that give rise to FAMs.⁴⁷

Finally, while AMF-like cells contribute to alveolar regeneration in the mouse influenza virus infection model, they appear to be aberrantly activated in non-resolving pneumonia in lethal ARDS in humans. *Bona fide* lung fibrosis has been described post-ARDS caused by SARS-CoV-2 or IAV.^{48–50} Given the transcriptomic similarity between AMF-like cells and FAMs,

it is plausible that the regenerative mechanism involving AMF-like cells might be hijacked to drive lung fibrosis instead of scarless regeneration in severe ARDS in humans. We recently showed that perivascular GLI1+ cells contribute to increased muscularization of the pulmonary vasculature in response to hypoxia or cigarette smoke exposure.⁵¹ We also showed that *GLI1* is upregulated in COPD lungs with pulmonary hypertension (PH). In the current work, we selected COPD lung tissues corresponding to patients with COPD but without PH, and the results showed significant downregulation of *GLI1* and *CTHRC1*. Therefore, our data showing the downregulation of markers of AMF-like cells mainly reflect the loss of alveolar structures and emphysema in the absence of vascular remodeling and PH and strongly suggest that the lack of AMF-like cells is associated with failed alveolar regeneration and emphysema.

To sum up, our work reveals that adult lung mesenchymal cells upregulate the developmental AMF gene signature during alveolar regeneration. Nevertheless, several questions remain open, including the cellular origin of AMF-like cells (other than the finding that they partially derive from GLI1+ cells), their actual function in repair and regeneration, and their main epithelial interacting partner(s) *in vivo*. Future research aimed at pinpointing the microenvironmental and molecular cues that control the behavior of these cells in terms of driving progressive remodeling and fibrosis versus balanced and scarless regeneration holds promise for developing innovative therapeutic strategies to promote alveolar regeneration in the diseased lung.

Limitations of the study

There are currently no transgenic or knockin mouse lines that allow exclusive labeling of AMFs without collateral labeling of other populations, such as SMCs or AFs. Moreover, while scRNA-seq deconvolutes the cellular heterogeneity of labeled populations and can also predict differentiation trajectories, it cannot determine, for example, whether neonatally labeled AMFs are themselves reactivated later in life. Future research using intersectional genetics will allow the neonatal labeling of a pure AMF population and following the fate of these cells during adulthood, therefore improving the temporal resolution of such investigations. Finally, it will be important, in the meantime, to select and validate surface markers that would allow selective sorting of AMFs and AMF-like cells for subsequent analysis.

Figure 5. AMF-like cells support AT2 growth *ex vivo*

(A and B) Timeline and experimental design. The datasets shown in Figure S4 were integrated with the mouse lung development atlas.⁴⁴
 (C–F) Cell-cell communication networks highlighting interactions between AMFs and AMF-like cells with other cell types. The thickness of the lines visualizes the strength of interactions.
 (G) Heatmap showing the top ligand-receptor interaction candidates. An extended list is shown in Data S1.
 (H) Timeline and experimental design for the generation of organoids.
 (I) Overview of wells with organoids at day 21 and immunofluorescence using indicated antibodies.
 (J) Quantification of organoid number and size.
 (H–J) $n = 6$ per group. (J) Data are represented as mean \pm SEM. *** $p < 0.0001$. Scale bars: (I) 1 mm for well overviews and 50 μ m for immunofluorescence. aCap, aerocytes; adventitial FB, adventitial fibroblasts; AMF, alveolar myofibroblasts; arterial maEC, macrovascular arterial endothelium; AT1, type 1 alveolar epithelial cells; AT2, type 2 alveolar epithelial cells; gCap, general capillary cells; i.p., intraperitoneal injection; PR8, A/Puerto Rico/8/34 H1N1; s.c., subcutaneous injection; Prolif. MyoFB, proliferative myofibroblasts; Tam, tamoxifen; venous maEC, macrovascular venous endothelium; Wnt2+ FB, Wnt2+ fibroblasts.
 See also Figures S2–S6 and Data S1.

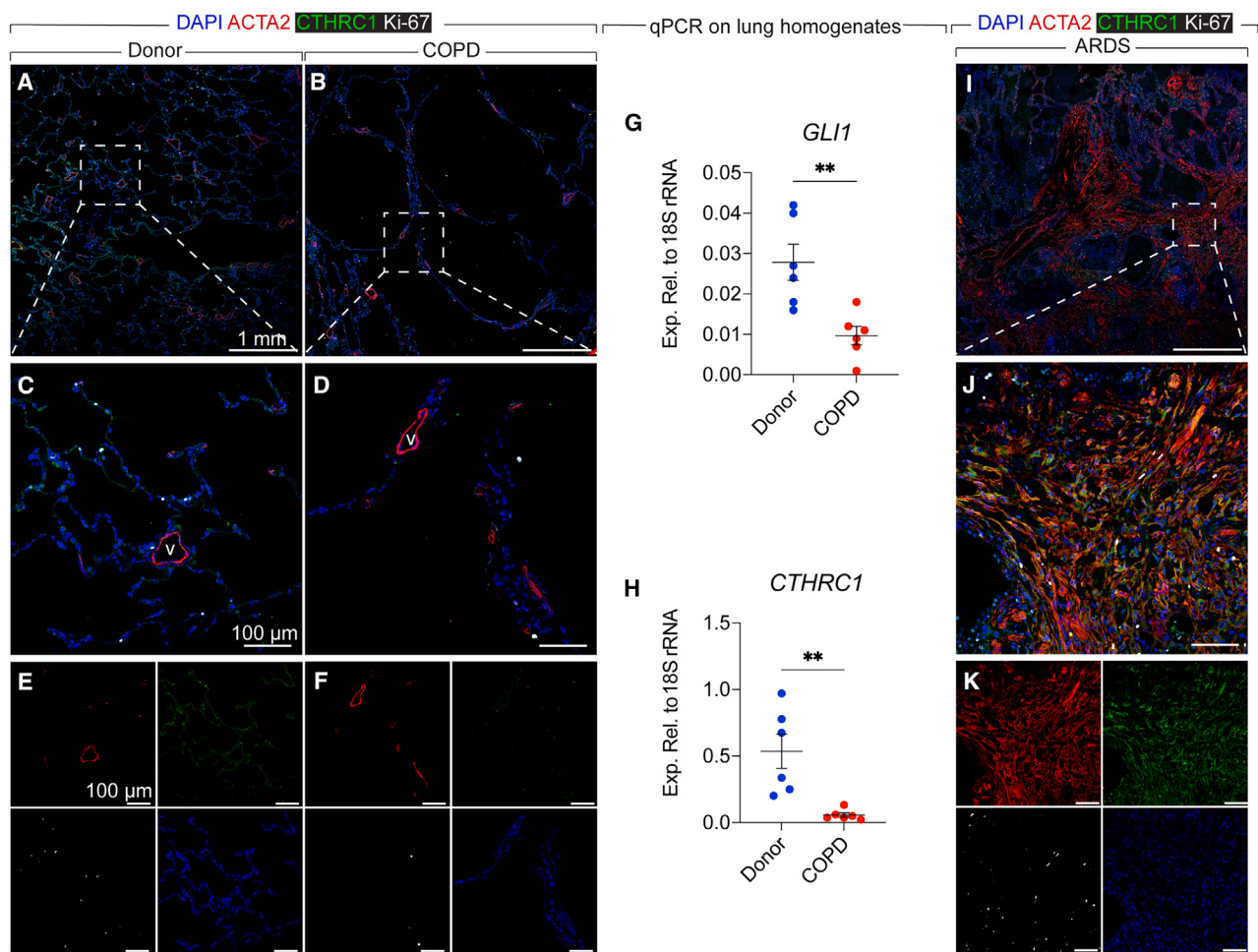


Figure 6. Dysregulation of AMF-like cells is associated with failed regeneration in the human lung

(A and B) Immunofluorescence using the indicated antibodies on donor and COPD lung explants.

(C and D) High-magnification images of the regions shown in the dashed boxes in (A) and (B). The letter "v" indicates blood vessels.

(E and F) Single-channel images of the regions shown in (C) and (D).

(G and H) Quantitative PCR on lung homogenates from donor and COPD lung samples.

(I) Immunofluorescence using the indicated antibodies on an ARDS lung autopsy.

(J) High-magnification image of the region shown in the dashed box in (I).

(K) Single-channel images of the region shown in (J).

(G and H) $n = 6$ per group. (G and H) Data are represented as mean \pm SEM. ** $p < 0.01$. Scale bars: (A, B, and I) 1 mm and (C–F, J, and K) 100 μ m. ARDS, acute respiratory distress syndrome; COPD, chronic obstructive pulmonary disease.

RESOURCE AVAILABILITY

Lead contact

Further information and requests for resources and reagents should be directed to and will be fulfilled by Elie El Agha (elie.el-agha@innere.med.uni-giessen.de).

Materials availability

This study did not generate new unique reagents.

Data and code availability

The bulk and scRNA-seq data were deposited on the Gene Expression Omnibus (GEO) under the accession number GEO: GSE248798 and are publicly available as of the date of publication. The dataset for mock *Glil1CreERT2*; *tdTomato*^{flx} was retrieved from GEO: GSE215094. Individual accession

numbers are listed in the [key resources table](#). This paper does not report original code. Any additional information required to reanalyze the data reported in this paper will be provided by the lead contact upon request. Other forms of raw data can be provided upon reasonable request.

ACKNOWLEDGMENTS

E.E.A. was funded by the German Research Foundation (DFG; EL 931/5-1, EL 931/4-1, EL 931/2-2 [KFO309 284237345], and SFB CRC1213 268555672), the Institute for Lung Health (ILH), the Excellence Cluster Cardio-Pulmonary Institute (EXC2026 390649896), and the German Center for Lung Research. The authors would like to thank Prof. Saverio Bellusci for contributing to generating the materials from pneumonectomized mice. The authors also thank Hannah Hofmann, Stefanie Jarmer, Florian Lück, Larissa Hamann, and Julia Stark for their technical support.

AUTHOR CONTRIBUTIONS

Conceptualization, E.E.A.; methodology, A.K., T.P.-K., D.G., T.M., X.C., A.M., M.B., I.K., S. Hadzic, and E.E.A.; investigation, A.K., G.K., A.I.V.-A., A.L., and E.E.A.; writing – original draft, A.K. and E.E.A.; writing – review & editing, A.K. and E.E.A.; funding acquisition, E.E.A.; resources, A.K., N.A., I.A., Y.C., A.G., J.B., J.N., H.B.S., X.L., N.W., T.B., W.S., M.W., R.E.M., S. Herold, and E.E.A.; supervision, E.E.A.

DECLARATION OF INTERESTS

The authors declare that they have no competing interests.

STAR★METHODS

Detailed methods are provided in the online version of this paper and include the following:

- **KEY RESOURCES TABLE**
- **EXPERIMENTAL MODEL AND STUDY PARTICIPANT DETAILS**
 - Mice and tamoxifen administration
 - Pneumonectomy
 - Influenza A virus-induced lung injury
 - Human samples
- **METHOD DETAILS**
 - Immunofluorescence
 - *In situ* hybridization
 - Flow cytometry analysis and cell sorting
 - Bulk RNA sequencing
 - Single-cell RNA sequencing
 - Alveolosphere assay
- **QUANTIFICATION AND STATISTICAL ANALYSIS**
- **ADDITIONAL RESOURCES**

SUPPLEMENTAL INFORMATION

Supplemental information can be found online at <https://doi.org/10.1016/j.celrep.2025.115248>.

Received: December 13, 2023

Revised: July 24, 2024

Accepted: January 9, 2025

Published: February 3, 2025

REFERENCES

1. El Agha, E., Seeger, W., and Bellusci, S. (2017). Therapeutic and pathological roles of fibroblast growth factors in pulmonary diseases. *Dev. Dynam.* 246, 235–244. <https://doi.org/10.1002/dvdy.24468>.
2. El Agha, E., and Bellusci, S. (2014). Walking along the Fibroblast Growth Factor 10 Route: A Key Pathway to Understand the Control and Regulation of Epithelial and Mesenchymal Cell-Lineage Formation during Lung Development and Repair after Injury. *Sci. Tech. Rep.* 2014, 538379. <https://doi.org/10.1155/2014/538379>.
3. El Agha, E., and Thannickal, V.J. (2023). The lung mesenchyme in development, regeneration, and fibrosis. *J. Clin. Invest.* 133, e170498. <https://doi.org/10.1172/JCI170498>.
4. Vaccaro, C., and Brody, J.S. (1978). Ultrastructure of developing alveoli. I. The role of the interstitial fibroblast. *Anat. Rec.* 192, 467–479. <https://doi.org/10.1002/ar.1091920402>.
5. Boström, H., Willetts, K., Pekny, M., Levéen, P., Lindahl, P., Hedstrand, H., Pekna, M., Hellström, M., Gebre-Medhin, S., Schalling, M., et al. (1996). PDGF-A signaling is a critical event in lung alveolar myofibroblast development and alveogenesis. *Cell* 85, 863–873.
6. Lindahl, P., Karlsson, L., Hellström, M., Gebre-Medhin, S., Willetts, K., Heath, J.K., and Betsholtz, C. (1997). Alveogenesis failure in PDGF-A-deficient mice is coupled to lack of distal spreading of alveolar smooth muscle cell progenitors during lung development. *Development* 124, 3943–3953.
7. Branchfield, K., Li, R., Lungova, V., Verheyden, J.M., McCullley, D., and Sun, X. (2016). A three-dimensional study of alveogenesis in mouse lung. *Dev. Biol.* 409, 429–441. <https://doi.org/10.1016/j.ydbio.2015.11.017>.
8. Endale, M., Ahlfeld, S., Bao, E., Chen, X., Green, J., Bess, Z., Weirauch, M.T., Xu, Y., and Perl, A.K. (2017). Temporal, spatial, and phenotypical changes of PDGFR α expressing fibroblasts during late lung development. *Dev. Biol.* 425, 161–175. <https://doi.org/10.1016/j.YDBIO.2017.03.020>.
9. Gouveia, L., Betsholtz, C., and Andrae, J. (2017). Expression analysis of platelet-derived growth factor receptor alpha and its ligands in the developing mouse lung. *Phys. Rep.* 5, e13092. <https://doi.org/10.14814/phy2.13092>.
10. Li, R., Bernau, K., Sandbo, N., Gu, J., Preissl, S., and Sun, X. (2018). Pdgfra marks a cellular lineage with distinct contributions to myofibroblasts in lung maturation and injury response. *Elife* 7, e36865. <https://doi.org/10.7554/elife.36865>.
11. McGowan, S.E., Grossmann, R.E., Kimani, P.W., and Holmes, A.J. (2008). Platelet-derived growth factor receptor-alpha-expressing cells localize to the alveolar entry ring and have characteristics of myofibroblasts during pulmonary alveolar septal formation. *Anat. Rec.* 291, 1649–1661. <https://doi.org/10.1002/ar.20764>.
12. Ntokou, A., Klein, F., Dontireddy, D., Becker, S., Bellusci, S., Richardson, W.D., Szibor, M., Braun, T., Morty, R.E., Seeger, W., et al. (2015). Characterization of the platelet-derived growth factor receptor-alpha-positive cell lineage during murine late lung development. *Am. J. Physiol. Lung Cell Mol. Physiol.* 309, L942–L958. <https://doi.org/10.1152/ajplung.00272.2014>.
13. Perl, A.-K.T., and Gale, E. (2009). FGF signaling is required for myofibroblast differentiation during alveolar regeneration. *Am. J. Physiol. Lung Cell Mol. Physiol.* 297, L299–L308. <https://doi.org/10.1152/ajplung.00008.2009>.
14. Lau, M., Masood, A., Yi, M., Belcastro, R., Li, J., and Tanswell, A.K. (2011). Long-term failure of alveogenesis after an early short-term exposure to a PDGF-receptor antagonist. *Am. J. Physiol. Lung Cell Mol. Physiol.* 300, L534–L547. <https://doi.org/10.1152/ajplung.00262.2010>.
15. Gouveia, L., Betsholtz, C., and Andrae, J. (2018). PDGF-A signaling is required for secondary alveolar septation and controls epithelial proliferation in the developing lung. *Development* 145, dev161976. <https://doi.org/10.1242/dev.161976>.
16. Li, C., Li, M., Li, S., Xing, Y., Yang, C.-Y., Li, A., Borok, Z., De Langhe, S., and Minoo, P. (2015). Progenitors of secondary crest myofibroblasts are developmentally committed in early lung mesoderm. *Stem Cell.* 33, 999–1012. <https://doi.org/10.1002/stem.1911>.
17. Moiseenko, A., Kheirollahi, V., Chao, C.-M., Ahmadvand, N., Quantius, J., Wilhelm, J., Herold, S., Ahlbrecht, K., Morty, R.E., Rizvanov, A.A., et al. (2017). Origin and characterization of alpha smooth muscle actin-positive cells during murine lung development. *Stem Cell.* 35, 1566–1578. <https://doi.org/10.1002/stem.2615>.
18. Zepp, J.A., Morley, M.P., Loebel, C., Kremp, M.M., Chaudhry, F.N., Basil, M.C., Leach, J.P., Liberti, D.C., Niethamer, T.K., Ying, Y., et al. (2021). Genomic, epigenomic, and biophysical cues controlling the emergence of the lung alveolus. *Science* 371, eabc3172. <https://doi.org/10.1126/science.abc3172>.
19. Gao, F., Li, C., Smith, S.M., Peinado, N., Kohbodi, G., Tran, E., Loh, E., Li, W., Borok, Z., and Minoo, P. (2022). Decoding the IGF1 Signaling Gene Regulatory Network Behind Alveogenesis from A Mouse Model of Bronchopulmonary Dysplasia. *Preprint at bioRxiv.* <https://doi.org/10.1101/2022.01.24.477613>.
20. He, H., Snowball, J., Sun, F., Na, C.-L., and Whitsett, J.A. (2021). IGF1R controls mechanosignaling in myofibroblasts required for pulmonary alveogenesis. *JCI Insight* 6, e144863. <https://doi.org/10.1172/jci.insight.144863>.

21. Hagan, A.S., Zhang, B., and Ornitz, D.M. (2020). Identification of a FGF18-expressing alveolar myofibroblast that is developmentally cleared during alveogenesis. *Development* 147, dev181032. <https://doi.org/10.1242/dev.181032>.
22. Narvaez Del Pilar, O., Gacha Garay, M.J., and Chen, J. (2022). Three-axis classification of mouse lung mesenchymal cells reveals two populations of myofibroblasts. *Development* 149, dev200081. <https://doi.org/10.1242/dev.200081>.
23. Kuang, P.-P., Lucey, E., Rishikof, D.C., Humphries, D.E., Bronsnick, D., and Goldstein, R.H. (2005). Engraftment of Neonatal Lung Fibroblasts into the Normal and Elastase-Injured Lung. *Am. J. Respir. Cell Mol. Biol.* 33, 371–377. <https://doi.org/10.1165/rcmb.2004-0319OC>.
24. Li, R., Li, X., Hagood, J., Zhu, M.-S., and Sun, X. (2020). Myofibroblast contraction is essential for generating and regenerating the gas-exchange surface. *J. Clin. Invest.* 130, 2859–2871. <https://doi.org/10.1172/jci132189>.
25. Kumar, P.A., Hu, Y., Yamamoto, Y., Hoe, N.B., Wei, T.S., Mu, D., Sun, Y., Joo, L.S., Dagher, R., Zielonka, E.M., et al. (2011). Distal airway stem cells yield alveoli in vitro and during lung regeneration following H1N1 influenza infection. *Cell* 147, 525–538. <https://doi.org/10.1016/j.cell.2011.10.001>.
26. Ray, S., Chiba, N., Yao, C., Guan, X., McConnell, A.M., Brockway, B., Que, L., McQualter, J.L., and Stripp, B.R. (2016). Rare SOX2+ Airway Progenitor Cells Generate KRT5+ Cells that Repopulate Damaged Alveolar Parenchyma following Influenza Virus Infection. *Stem Cell Rep.* 7, 817–825. <https://doi.org/10.1016/j.stemcr.2016.09.010>.
27. Salwig, I., Spitznagel, B., Vazquez-Armendariz, A.I., Khalooghi, K., Guenther, S., Herold, S., Szibor, M., and Braun, T. (2019). Bronchioalveolar stem cells are a main source for regeneration of distal lung epithelia in vivo. *EMBO J.* 38, 1–16. <https://doi.org/10.1525/embj.2019102099>.
28. Strunz, M., Simon, L.M., Ansari, M., Kathiriy, J.J., Angelidis, I., Mayr, C.H., Tsidiridis, G., Lange, M., Matthner, L.F., Yee, M., et al. (2020). Alveolar regeneration through a Krt8+ transitional stem cell state that persists in human lung fibrosis. *Nat. Commun.* 11, 3559. <https://doi.org/10.1038/s41467-020-17358-3>.
29. Vaughan, A.E., Brumwell, A.N., Xi, Y., Gotts, J.E., Brownfield, D.G., Treutlein, B., Tan, K., Tan, V., Liu, F.C., Looney, M.R., et al. (2015). Lineage-negative progenitors mobilize to regenerate lung epithelium after major injury. *Nature* 517, 621–625. <https://doi.org/10.1038/nature14112>.
30. Zacharias, W.J., Frank, D.B., Zepp, J.A., Morley, M.P., Alkhaleel, F.A., Kong, J., Zhou, S., Cantu, E., and Morrissey, E.E. (2018). Regeneration of the lung alveolus by an evolutionarily conserved epithelial progenitor. *Nature* 555, 251–255. <https://doi.org/10.1038/nature25786>.
31. Quantius, J., Schmoldt, C., Vazquez-Armendariz, A.I., Becker, C., El Agha, E., Wilhelm, J., Morty, R.E., Vadász, I., Mayer, K., Gattenloehner, S., et al. (2016). Influenza Virus Infects Epithelial Stem/Progenitor Cells of the Distal Lung: Impact on Fgrf2b-Driven Epithelial Repair. *PLoS Pathog.* 12, e1005544. <https://doi.org/10.1371/journal.ppat.1005544>.
32. Paris, A.J., Hayer, K.E., Oved, J.H., Avgousti, D.C., Toulmin, S.A., Zepp, J.A., Zacharias, W.J., Katzen, J.B., Basil, M.C., Kremp, M.M., et al. (2020). STAT3-BDNF-TrkB signalling promotes alveolar epithelial regeneration after lung injury. *Nat. Cell Biol.* 22, 1197–1210. <https://doi.org/10.1038/s41556-020-0569-x>.
33. Boyd, D.F., Allen, E.K., Randolph, A.G., Guo, X.Z.J., Weng, Y., Sanders, C.J., Bajracharya, R., Lee, N.K., Guy, C.S., Vogel, P., et al. (2020). Exuberant fibroblast activity compromises lung function via ADAMTS-4. *Nature* 587, 466–471. <https://doi.org/10.1038/s41586-020-2877-5>.
34. Tsukui, T., Sun, K.-H., Wetter, J.B., Wilson-Kanamori, J.R., Hazelwood, L.A., Henderson, N.C., Adams, T.S., Schupp, J.C., Poli, S.D., Rosas, I.O., et al. (2020). Collagen-producing lung cell atlas identifies multiple subsets with distinct localization and relevance to fibrosis. *Nat. Commun.* 11, 1920. <https://doi.org/10.1038/s41467-020-15647-5>.
35. Xie, T., Liang, J., Liu, N., Huan, C., Zhang, Y., Liu, W., Kumar, M., Xiao, R., D'Armiento, J., Metzger, D., et al. (2016). Transcription factor TBX4 regulates myofibroblast accumulation and lung fibrosis. *J. Clin. Invest.* 126, 3626. <https://doi.org/10.1172/JCI89968>.
36. El Agha, E., Moiseenko, A., Kheirollahi, V., De Langhe, S., Crnkovic, S., Kwapiszewska, G., Szibor, M., Kosanovic, D., Schwind, F., Schermuly, R.T., et al. (2017). Two-Way Conversion between Lipogenic and Myogenic Fibroblastic Phenotypes Marks the Progression and Resolution of Lung Fibrosis. *Cell Stem Cell* 20, 261–273. <https://doi.org/10.1016/j.stem.2016.10.004>.
37. Mayr, C.H., Sengupta, A., Asgharpour, S., Ansari, M., Pestoni, J.C., Ogar, P., Angelidis, I., Lontos, A., Rodriguez-Castillo, J.A., Lang, N.J., et al. (2024). Sfrp1 inhibits lung fibroblast invasion during transition to injury induced myofibroblasts. *Eur. Respir. J.* 63, 2301326. <https://doi.org/10.1183/13993003.01326-2023>.
38. Trempus, C.S., Papas, B.N., Sifre, M.I., Bortner, C.D., Scappini, E., Tucker, C.J., Xu, X., Johnson, K.L., Deterding, L.J., Williams, J.G., et al. (2023). Functional PDGFR α fibroblast heterogeneity in normal and fibrotic mouse lung. *JCI Insight* 8, e164380. <https://doi.org/10.1172/jci.insight.164380>.
39. Tsukui, T., Wolters, P.J., and Sheppard, D. (2024). Alveolar fibroblast lineage orchestrates lung inflammation and fibrosis. *Nature* 631, 627–634. <https://doi.org/10.1038/s41586-024-07660-1>.
40. Al Alam, D., El Agha, E., Sakurai, R., Kheirollahi, V., Moiseenko, A., Danopoulos, S., Shrestha, A., Schmoldt, C., Quantius, J., Herold, S., et al. (2015). Evidence for the involvement of fibroblast growth factor 10 in lipofibroblast formation during embryonic lung development. *Development* 142, 4139–4150. <https://doi.org/10.1242/dev.109173>.
41. Chu, X., Taghizadeh, S., Vazquez-Armendariz, A.I., Herold, S., Chong, L., Chen, C., Zhang, J.-S., El Agha, E., and Bellusci, S. (2021). Validation of a Novel Fgf10 Cre-ERT2 Knock-in Mouse Line Targeting FGF10Pos Cells Postnatally. *Front. Cell Dev. Biol.* 9, 671841. <https://doi.org/10.3389/fcell.2021.671841>.
42. El Agha, E., Herold, S., Al Alam, D., Quantius, J., MacKenzie, B., Carraro, G., Moiseenko, A., Chao, C.-M., Minoo, P., Seeger, W., and Bellusci, S. (2014). Fgf10-positive cells represent a progenitor cell population during lung development and postnatally. *Development* 141, 296–306. <https://doi.org/10.1242/dev.099747>.
43. El Agha, E., Al Alam, D., Carraro, G., MacKenzie, B., Goth, K., De Langhe, S.P., Voswinckel, R., Hajhosseini, M.K., Rehan, V.K., and Bellusci, S. (2012). Characterization of a novel fibroblast growth factor 10 (Fgf10) knock-in mouse line to target mesenchymal progenitors during embryonic development. *PLoS One* 7, e38452. <https://doi.org/10.1371/journal.pone.0038452>.
44. Negretti, N.M., Plosa, E.J., Benjamin, J.T., Schuler, B.A., Habermann, A.C., Jetter, C.S., Gulleman, P., Bunn, C., Hackett, A.N., Ransom, M., et al. (2021). A single-cell atlas of mouse lung development. *Development* 148, dev199512. <https://doi.org/10.1242/dev.199512>.
45. Gao, F., Li, C., Danopoulos, S., Al Alam, D., Peinado, N., Webster, S., Borok, Z., Kohbodi, G.A., Bellusci, S., and Minoo, P. (2022). Hedgehog-responsive PDGFR α (+) fibroblasts maintain a unique pool of alveolar epithelial progenitor cells during alveogenesis. *Cell Rep.* 39, 110608. <https://doi.org/10.1016/j.celrep.2022.110608>.
46. Chandran, R.R., Adams, T.S., Kabir, I., Gallardo-Vara, E., Kaminski, N., Gomperts, B.N., and Greif, D.M. (2024). Dedifferentiated early postnatal lung myofibroblasts redifferentiate in adult disease. *Front. Cell Dev. Biol.* 12, 1335061. <https://doi.org/10.3389/fcell.2024.1335061>.
47. Konkimalla, A., Konishi, S., Macadlo, L., Kobayashi, Y., Farino, Z.J., Miyashita, N., El Haddad, L., Morowitz, J., Barkauskas, C.E., Agarwal, P., et al. (2023). Transitional cell states sculpt tissue topology during lung regeneration. *Cell Stem Cell* 30, 1486–1502. <https://doi.org/10.1016/j.stem.2023.10.001>.
48. Burnham, E.L., Janssen, W.J., Riches, D.W.H., Moss, M., and Downey, G.P. (2014). The fibroproliferative response in acute respiratory distress syndrome: mechanisms and clinical significance. *Eur. Respir. J.* 43, 276–285. <https://doi.org/10.1183/09031936.00196412>.
49. Mineo, G., Ciccarese, F., Modolon, C., Landini, M.P., Valentino, M., and Zompatori, M. (2012). Post-ARDS pulmonary fibrosis in patients with

- H1N1 pneumonia: role of follow-up CT. *Radiol. Med.* **117**, 185–200. <https://doi.org/10.1007/s11547-011-0740-3>.
50. Wendisch, D., Dietrich, O., Mari, T., von Stillfried, S., Ibarra, I.L., Mittermaier, M., Mache, C., Chua, R.L., Knoll, R., Timm, S., et al. (2021). SARS-CoV-2 infection triggers profibrotic macrophage responses and lung fibrosis. *Cell* **184**, 6243–6261. <https://doi.org/10.1016/j.cell.2021.11.033>.
51. Chu, X., Kheirollahi, V., Lingampally, A., Chelladurai, P., Valasaranjan, C., Vazquez-Armendariz, A.I., Hadzic, S., Khadim, A., Pak, O., Rivetti, S., et al. (2024). GLI1+ Cells Contribute to Vascular Remodeling in Pulmonary Hypertension. *Circ. Res.* **134**, e133–e149. <https://doi.org/10.1161/CIRCRESAHA.123.323736>.
52. Chu, X., Lingampally, A., Moiseenko, A., Kheirollahi, V., Vazquez-Armenadariz, A.I., Koepke, J., Khadim, A., Kiliaris, G., Shahriari Felordi, M., Zabihi, M., et al. (2022). GLI1+ cells are a source of repair-supportive mesenchymal cells (RSMCs) during airway epithelial regeneration. *Cell. Mol. Life Sci.* **79**, 581. <https://doi.org/10.1007/s00018-022-04599-2>.
53. Ahmadvand, N., Khosravi, F., Lingampally, A., Wasnick, R., Vazquez-Armenadariz, A.I., Carraro, G., Heiner, M., Rivetti, S., Lv, Y., Wilhelm, J., et al. (2021). Identification of a novel subset of alveolar type 2 cells enriched in PD-L1 and expanded following pneumonectomy. *Eur. Respir. J.* **58**, 2004168. <https://doi.org/10.1183/13993003.04168-2020>.
54. Schindelin, J., Arganda-Carreras, I., Frise, E., Kaynig, V., Longair, M., Pietzsch, T., Preibisch, S., Rueden, C., Saalfeld, S., Schmid, B., et al. (2012). Fiji: an open-source platform for biological-image analysis. *Nat. Methods* **9**, 676–682. <https://doi.org/10.1038/nmeth.2019>.
55. Ewels, P.A., Peltzer, A., Fillinger, S., Patel, H., Alneberg, J., Wilm, A., Garcia, M.U., Di Tommaso, P., and Nahnsen, S. (2020). The nf-core framework for community-curated bioinformatics pipelines. *Nat. Biotechnol.* **38**, 276–278. <https://doi.org/10.1038/s41587-020-0439-x>.
56. Yu, G., Wang, L.-G., Han, Y., and He, Q.-Y. (2012). clusterProfiler: an R package for comparing biological themes among gene clusters. *OMICS* **16**, 284–287. <https://doi.org/10.1089/omi.2011.0118>.
57. Wolf, F.A., Angerer, P., and Theis, F.J. (2018). SCANPY: large-scale single-cell gene expression data analysis. *Genome Biol.* **19**, 15. <https://doi.org/10.1186/s13059-017-1382-0>.
58. Han, X., Wang, R., Zhou, Y., Fei, L., Sun, H., Lai, S., Saadatpour, A., Zhou, Z., Chen, H., Ye, F., et al. (2018). Mapping the Mouse Cell Atlas by Microwell-Seq. *Cell* **172**, 1091–1107. <https://doi.org/10.1016/j.cell.2018.02.001>.
59. Wu, T., Hu, E., Xu, S., Chen, M., Guo, P., Dai, Z., Feng, T., Zhou, L., Tang, W., Zhan, L., et al. (2021). clusterProfiler 4.0: A universal enrichment tool for interpreting omics data. *Innovation* **2**, 100141. <https://doi.org/10.1016/j.xinn.2021.100141>.
60. Bergen, V., Lange, M., Peidli, S., Wolf, F.A., and Theis, F.J. (2020). Generalizing RNA velocity to transient cell states through dynamical modeling. *Nat. Biotechnol.* **38**, 1408–1414. <https://doi.org/10.1038/s41587-020-0591-3>.
61. Ge, S.X., Jung, D., and Yao, R. (2020). ShinyGO: a graphical gene-set enrichment tool for animals and plants. *Bioinformatics* **36**, 2628–2629. <https://doi.org/10.1093/bioinformatics/btz931>.
62. Hao, Y., Hao, S., Andersen-Nissen, E., Mauck, W.M., Zheng, S., Butler, A., Lee, M.J., Wilk, A.J., Darby, C., Zager, M., et al. (2021). Integrated analysis of multimodal single-cell data. *Cell* **184**, 3573–3587. <https://doi.org/10.1016/j.cell.2021.04.048>.
63. Jin, S., Guerrero-Juarez, C.F., Zhang, L., Chang, I., Ramos, R., Kuan, C.-H., Myung, P., Plikus, M.V., and Nie, Q. (2021). Inference and analysis of cell-cell communication using CellChat. *Nat. Commun.* **12**, 1088. <https://doi.org/10.1038/s41467-021-21246-9>.

STAR★METHODS

KEY RESOURCES TABLE

REAGENT or RESOURCE	SOURCE	IDENTIFIER
Antibodies		
Mouse monoclonal anti-Actin, α -Smooth Muscle - FITC antibody produced in mouse	Sigma	Cat# F3777-.2ML; RRID:AB_476977
α -Actin Antibody (1A4) Alexa Fluor® 647	Santa Cruz Biotechnology	Cat# sc-32251 AF647; RRID: AB_3661645
Rabbit monoclonal anti-PDGFR alpha antibody [EPR22059-270]	Abcam	Cat# ab203491; RRID:AB_2892065
Mouse monoclonal anti-KI67 antibody	Cell signaling Technology	Cat# 9449s; RRID:AB_2797703
Rabbit polyclonal anti-KI67 antibody	Thermo Fisher Scientific	Cat# PA5-19462; RRID:AB_10981523
Rat monoclonal anti-RAGE	R&D System	Cat# MAB1179; RRID:AB_2289349
Sheep polyclonal anti-CTHRC1	R&D System	Cat# AF5960; RRID:AB_1964549
Rat monoclonal anti-CD45	Biolegend	Cat# 103102; RRID:AB_312967
Chicken Polyclonal anti-Keratin 5 Antibody	Biolegend	Cat# 905904; RRID:AB_2721743
Rabbit polyclonal anti-Pro-SP-C antibody	Seven Hills	Cat# WRAB-9337; RRID:AB_2335890
Goat anti-Mouse IgG (H + L) Cross-Adsorbed Secondary Antibody, Alexa Fluor 488	Thermo Fisher Scientific	Cat# A-11001; RRID:AB_2534069
Donkey anti-Mouse IgG (H + L) Highly Cross-Adsorbed Secondary Antibody, Alexa Fluor 647	Thermo Fisher Scientific	Cat# A-31571; RRID:AB_162542
Goat anti-Rabbit IgG (H + L) Cross-Adsorbed Secondary Antibody, Alexa Fluor 488	Thermo Fisher Scientific	Cat# A-11008; RRID:AB_143165
Goat anti-Rabbit IgG (H + L) Highly Cross-Adsorbed Secondary Antibody, Alexa Fluor 647	Thermo Fisher Scientific	Cat# A-21245; RRID:AB_2535813
Donkey anti-Rabbit IgG (H + L) Highly Cross-Adsorbed Secondary Antibody, Alexa Fluor Plus 488	Thermo Fisher Scientific	Cat# A32790; RRID:AB_2762833
Donkey anti-Rabbit IgG (H + L) Highly Cross-Adsorbed Secondary Antibody, Alexa Fluor 647	Thermo Fisher Scientific	Cat# A-31573; RRID:AB_2536183
Chicken anti-Rat IgG (H + L) Cross-Adsorbed Secondary Antibody, Alexa Fluor 488	Thermo Fisher Scientific	Cat# A-21470; RRID:AB_2535873
Goat anti-Rat IgG (H + L) Cross-Adsorbed Secondary Antibody, Alexa Fluor™ 647	Thermo Fisher Scientific	Cat# A-21247; RRID:AB_141778
Donkey anti-Sheep IgG (H + L) Cross-Adsorbed Secondary Antibody, Alexa Fluor™ 488	Thermo Fisher Scientific	Cat# A-11015; RRID:AB_141362
Donkey anti-Sheep IgG (H + L) Cross-Adsorbed Secondary Antibody, Alexa Fluor™ 647	Thermo Fisher Scientific	Cat# A-21448; RRID:AB_2535865

(Continued on next page)

Continued

REAGENT or RESOURCE	SOURCE	IDENTIFIER
Pacific Blue™ anti-mouse Ly-6A/E (Sca-1) Antibody	Biolegend	Cat# 108120; RRID:AB_493273
APC/Cy7 anti-mouse CD326 (Ep-CAM) Antibody	Biolegend	Cat# 118218; RRID:AB_2098648
APC anti-mouse CD140a Antibody	Biolegend	Cat# 135908; RRID:AB_2043970
Alexa Fluor® 488 anti-mouse CD45 Antibody	BioLegend	Cat# 103122; RRID:AB_493531
Alexa Fluor® 488 anti-mouse CD31 Antibody	BioLegend	Cat# 102514; RRID:AB_2161031
APC anti-mouse Sca-1 Antibody	Biolegend	Cat# 108112; RRID:AB_313349
Bacterial and virus strains		
Influenza A virus PR8 (A/PR/8/1934(H1N1))	ATCC	Cat# VR-95
Chemicals, peptides, and recombinant proteins		
DAPI (4',6-Diamidino-2-Phenylindole, Dihydrochloride)	Thermo Fisher	Cat# D1306
Bovine Serum Albumin (IgG-Free, Protease-Free)	Jackson ImmunoResearch	Cat# 001-000-162
Tamoxifen powder	Sigma	Cat# T5648-1G
Corn oil	Sigma	Cat# C8267-500ML
Fluoromount-G®	Southern Biotech	Cat# 0100-01
Bovine Serum Albumin (IgG-Free, Protease-Free)	Jackson ImmunoResearch	Cat# 001-000-162
ProLong™ Gold Antifade Mountant with DAPI	Thermo Fisher	Cat# P36931
Kollagenase, Typ IV, Pulver	Thermo Fisher Scientific	Cat# 17104019
UltraPure LMP Agarose	Invitrogen	Cat# 16520-100
PBS (phosphatgepufferte Salzlösung) (10X) pH 7.4	Thermo Fisher Scientific	Cat# 70011044
Critical commercial assays		
H&E fast staining kit, 2 x 500 mL	Carl Roth	Cat# 9194.2
Chromium Next GEM Chip G Single Cell Kit, 48 rxns	10x Genomics	Cat# 1000120
Chromium Next GEM Single Cell 3' GEM, Library & Gel Bead Kit v3.1, 16 rxns	10x Genomics	Cat# 1000268
10X Genomics Inc Single Index Kit T Set A	10x Genomics	Cat# 1000213
RNeasy Mini Kit	Qiagen	Cat# 74104
Deposited data		
Transcriptomic profiling of lineage-labeled and mesenchymal cells under various conditions	This study	GEO: GSE248798 https://www.ncbi.nlm.nih.gov/geo/query/acc.cgi?acc=GSE248798
Single-cell RNA-seq of alveolar myofibroblasts and other clusters	This study	GEO: GSE248726 https://www.ncbi.nlm.nih.gov/geo/query/acc.cgi?acc=GSE248726
Bulk RNA-seq of murine lung mesenchymal cells sorted after day 7 and day 14 of sham or pneumonectomy	This study	GEO: GSE248797 https://www.ncbi.nlm.nih.gov/geo/query/acc.cgi?acc=GSE248797
GLI1+ cells are a source of repair-supportive mesenchymal cells (RSMCs) during airway epithelial regeneration	Chu et al. ⁵²	GEO: GSE215094 https://www.ncbi.nlm.nih.gov/geo/query/acc.cgi?acc=GSE215094

(Continued on next page)

Continued

REAGENT or RESOURCE	SOURCE	IDENTIFIER
Single cell RNA-sequencing of normal and fibrotic lungs in mouse and human	Tsukui et al. ³⁴	GEO: GSE132771 https://www.ncbi.nlm.nih.gov/geo/query/acc.cgi?acc=GSE132771
The single-cell atlas of mouse lung development	Negretti et al. ⁴⁴	GEO: GSE165063 https://www.ncbi.nlm.nih.gov/geo/query/acc.cgi?acc=GSE165063
Experimental models: Organisms/strains		
C57BL/6J	Charles River Laboratories	Cat# 2498079-86; RRID: MGI:3028467
Tg(Acta2-cre/ERT2)12Pcn		MGI:3831907
Gli1 ^{tm3(Cre/ERT2)Alj} /J	Jackson Laboratory	Cat# 007913; RRID: IMSR_JAX:007913
B6; 129S6-Gt(ROSA)26Sor ^{tm1(CAG-tdTomato)Hze} /J	Jackson Laboratory	Cat# 007905; RRID: IMSR_JAX:007905
Oligonucleotides		
GLI1 F: AGCCTTCAGCAATGCCAGTGAC	Origene	Cat# HP208438; Uniport ID: P08151
GLI1 R: GTCAGGACCATGCACTGTCTTG		
CTHRC1 F: CAGGACCTCTTCCCATTGAAGC	Origene	Cat# HP217001; Uniport ID: Q96CG8
CTHRC1 R: GCAACATCCACTAATCCAGCACC		
Software and algorithms		
FlowJo v10.10	BD Biosciences https://www.flowjo.com/solutions/flowjo	RRID: SCR_008520
FIJI	https://imagej.net/software/fiji/	RRID: SCR_002285
IMARIS	https://imaris.oxinst.com/	RRID: SCR_007370
Leica Application Suite X	https://www.leica-microsystems.com/products/microscope-software/p/leica-las-x-ls/	RRID: SCR_013673
STAR	http://code.google.com/p/rna-star/	RRID: SCR_004463
clusterProfiler	https://bioconductor.org/packages/release/bioc/html/clusterProfiler.html	RRID: SCR_016884
Scanpy (v1.8.1)	https://pypi.org/project/scanpy/	RRID: SCR_018139
Scrublet	https://github.com/swolock/scrublet	RRID: SCR_018098
Anndata	https://github.com/scverse/anndata	RRID: SCR_018209
Harmony	https://github.com/immunogenomics/harmony	RRID: SCR_022206
Python (v3.8.10)	https://www.python.org/downloads/release/python-3810/	RRID: SCR_008394
cellxgene	https://github.com/chanzuckerberg/cellxgene	RRID: SCR_021059
scVelo	https://github.com/theislab/scvelo	RRID: SCR_018168
Seurat	https://satijalab.org/seurat/	RRID: SCR_016341
RStudio	https://posit.co/download/rstudio-desktop/	RRID: SCR_000432
sctransform	https://github.com/satijalab/sctransform	RRID: SCR_022146
scMCA	https://github.com/ggilab/scMCA	
DESeq2	https://bioconductor.org/packages/release/bioc/html/DESeq2.html	RRID: SCR_015687
fgsea	https://bioconductor.org/packages/release/bioc/html/fgsea.html	RRID: SCR_020938

(Continued on next page)

Continued

REAGENT or RESOURCE	SOURCE	IDENTIFIER
ComplexHeatmap	https://bioconductor.org/packages/release/bioc/html/ComplexHeatmap.html	RRID:SCR_017270
ShinyGO	http://bioinformatics.sdsstate.edu/go/	RRID:SCR_019213
CellChat	https://github.com/sqjin/CellChat	RRID:SCR_021946
KEGG	https://www.genome.jp/kegg/	RRID:SCR_012773
GraphPad Prism	GraphPad https://www.graphpad.com/	RRID:SCR_002798
Illustrator CS6	https://www.adobe.com/de/products/illustrator.html#modal-hash	RRID:SCR_010279

EXPERIMENTAL MODEL AND STUDY PARTICIPANT DETAILS

Mice and tamoxifen administration

All animal studies were performed according to protocols approved by the Animal Ethics Committee of Justus Liebig University Giessen and by the local authorities (Regierungspräsidium Giessen). Mice were housed in a specific pathogen-free (SPF) environment with unrestricted access to food and water. *Acta2-Cre-ERT2* mice (STOCK Tg(Acta2-cre/ERT2)12Pcn) were generously provided by Dr. Pierre Chambon from the University of Strasbourg, France. *Gli1^{Cre-ERT2}* mice (STOCK Gli1^{tm3(cre/ERT2)Alj}/J, JAX stock number 007913) and *tdTomato*^{flox} mice (B6; 129S6-Gt(ROSA)26Sor^{tm1(CAG-tdTomato)Hze}/J) (JAX stock number 007905) were purchased from the Jackson Laboratory. To induce Cre-ERT2-mediated genetic recombination, mice were exposed to tamoxifen as described in the corresponding figure legends. For subcutaneous (s.c.) or intraperitoneal (i.p.) injections, tamoxifen stock (20 mg/mL) was prepared by dissolving tamoxifen powder in corn oil (both from Sigma) and administered at a dose of 0.5 mg per pup at postnatal day 4 (P4) (approval number G83/2017) or 0.1 mg/g body weight in the adult stage (approval number G57/2021), respectively.

Pneumonectomy

The samples used to analyze AMFs in sham and pneumonectomized mice were generated in a previous study.⁵³ Briefly, C57BL6 mice were subjected to surgery (sham or pneumonectomy (PNX)) at 8–12 weeks of age. In the PNX group, the left lung lobe was resected while in the sham control group, thoracotomy was performed without lung removal. At days 7 and 14 post-surgery, mice were euthanized, and lungs were isolated. The left lobe was excluded from the analysis in the sham group to maintain consistency with the PNX group, which had the left lobe removed.

Influenza A virus-induced lung injury

Mice were anesthetized and intratracheally inoculated with 400 focus forming units (FFU) of influenza A/PR/8/34 (PR8; a mouse adapted H1N1 influenza virus). The virus was diluted in sterile PBS to a total volume of 70 µL. These experiments were approved by the local authorities (approval number G57/2021).

Human samples

Human donor and COPD biospecimen were provided by the UGMLC Giessen Biobank, member of the DZL Platform Biobanking. These samples were subjected to RNA extraction followed by qPCR as well as immunofluorescence. Human ARDS biospecimen were obtained from the CPC-M bioArchive at the Comprehensive Pneumology Center (CPC), Munich, and were subjected to immunofluorescence.

METHOD DETAILS

Immunofluorescence

Lungs were flushed by transcardiac perfusion with PBS. Subsequently, different protocols were followed based on the intended analysis. For paraffin embedding, lungs were fixed in 4% paraformaldehyde (PFA) and for cryosectioning, lungs were embedded in 5% OCT. Blocks were eventually sectioned into 5 µm-thick slices using a microtome or cryotome. For sectioning with a vibratome, lungs were inflated with 1.5% low melting agarose (Sigma), and 200 µm sections were obtained. Immunofluorescence (IF) was performed using monoclonal anti-ACTA2 (Sigma, 1:100 or Santa Cruz 1:200), polyclonal anti-PDGFR α (Abcam, 1:200), monoclonal anti-KI-67 (Cell Signaling Technology, 1:200), polyclonal anti-KI-67 (Thermo Fisher Scientific, 1:200), polyclonal anti-CTHRC1 (R&D System 1:100), monoclonal anti-RAGE (R&D System 1:400), polyclonal anti-SFTPC (Seven Hills, 1:1000), and polyclonal anti-RFP antibodies (Thermo Fisher Scientific, 1:200; used only in combination with KI-67 staining, which requires antigen retrieval). Neural lipids were stained using LipidTOX (Thermo Fisher Scientific, 1:200) and nuclei were stained using 4',6-Diamidino-2-Phenylindole, Dihydrochloride (DAPI) (Life Technologies). The catalog numbers of the antibodies and other key reagents are provided in the

Key resources table. Fluorescent images were acquired using either a Leica DM550 B fluorescence microscope or an SP8 confocal microscope equipped with a white-light laser and hybrid detectors or a Mica Widefocal LiveCell System (Leica Microsystems). When applicable, three-dimensional (3D) reconstruction of z-stacks was performed using the 3D module of LAS X software (version 3.5; Leica Microsystems). Image quantification was conducted using Fiji⁵⁴ and Imaris software (Oxford Instruments). For quantification, sections from at least 3 independent lungs were analyzed, and multiple images were used ($n > 8$) for stained control and experimental lungs.

In situ hybridization

Lung samples were embedded in Tissue-Tek OCT compound (#4583, Sakura) and sectioned at a thickness of 5 μm using Superfrost Plus microscope slides (#03–0060, R. Langenbrinck GmbH). *Cthrc1* and *Piezo2* transcripts were detected using specific probes (Mm-Cthrc1 Cat. # 413341 and Mm-Piezo2-C3 Cat. # 400191-C3, respectively), and the RNAscope Multiplex Fluorescent Reagent Kit v2 assay (document Nr:323100-USM, Advanced Cell Diagnostic) was employed according to the manufacturer's instructions. Upon completion of the RNAscope protocol, slides were washed with PBST buffer at room temperature for 5 min. ACTA2 immunofluorescence staining was performed using monoclonal anti-ACTA2 antibodies (Sigma) for 3 h at room temperature. After staining, samples were counterstained with DAPI (Life Technologies). Finally, the samples were mounted with Fluoromount (SouthernBiotech), and images were acquired using Mica (Leica).

Flow cytometry analysis and cell sorting

Flow cytometry and cell sorting procedures were performed according to standard procedures. Briefly, lungs were isolated and placed in Hank's Balanced Salt Solution (HBSS, Gibco). They were then minced into small pieces and incubated with 0.5% collagenase type IV in HBSS (Life Technologies) at 37°C for 45 min. Subsequently, lung homogenates were filtered through 70 μm and 40 μm cell strainers (BD Biosciences) to obtain single-cell suspensions. Cells were then centrifuged at 4°C at 1000 rpm for 5 min and resuspended in MACS buffer. Following that, cells were stained with anti-Ly6a (APC-conjugated, 1:50), anti-EpCAM (APC-Cy7-conjugated, 1:50), anti-CD31 (FITC-conjugated, 1:100), and anti-CD45 (FITC-conjugated, 1:100) antibodies (all from Biolegend) for 25 min on ice in the dark. Subsequently, cells were washed with MACS buffer. Flow cytometry and cell sorting were performed using a FACSaria III cell sorter (BD Biosciences), and live cells were gated using SyTOX (1:1000). Data were analyzed using FlowJo software (FlowJo LLC).

Bulk RNA sequencing

For analyzing gene expression following sham or PNX, FACS-sorted mesenchymal cells defined as CD45^{neg} CD31^{neg} EpCAM^{neg} (non-leukocytic, non-endothelial, non-epithelial) cells were centrifuged at 300 G for 10 min and subjected to RNA extraction using the RNeasy Microkit (Qiagen). Bulk RNA sequencing (Bulk RNA-seq) was carried out according to standard procedures. For genome-wide analysis of gene expression, RNA sequencing libraries from polyadenylated mRNA were generated and sequenced by the Institute for Lung Health (ILH) – Genomics and Bioinformatics – at the Justus-Liebig-University (JLU) Giessen (Germany). A total amount of 2–10 ng of RNA per sample was used for cDNA sequencing library preparation utilizing the NEBNext Single Cell/Low Input RNA Library Prep Kit for Illumina (New England BioLabs) according to the manufacturer's instructions. After library quality control by capillary electrophoresis (4200 TapeStation, Agilent), cDNA libraries were sequenced on the Illumina NovaSeq 6000 platform generating 50 bp paired-end reads. For demultiplexing and the subsequent FASTQ file generation we used Illumina's bcl2fastq (2.19.0.316). Primary processing of the sequencing reads, i.e., quality control, filtering, trimming, read alignment and generation of gene specific count tables was performed using the nf-core⁵⁵ RNA-seq v3.7 bioinformatics pipeline (NEXTFLOW version 23.04.03). The *mus musculus* mm10 genome and gene annotation was used as downloaded from Illumina's iGenome repository (https://support.illumina.com/sequencing/sequencing_software/igenome.html). The pipeline run was performed with standard parameters in docker mode. The resulting tables with raw read counts were imported into R where all down-stream processing was performed (R Core Team (2022) R: A Language and Environment for Statistical Computing. R Foundation for Statistical Computing, Vienna. URL <https://www.R-project.org/>). Normalization and detection of differentially expressed genes was determined using DESeq2. Gene set enrichment analysis was done using clusterProfiler and fgsea packages in R⁵⁶ using GO and KEGG annotations. All analysis code is available upon request.

Single-cell RNA sequencing

Single-cell RNA-seq (scRNA-seq) of tdTomato+ (tdTom+) cells FACS-sorted from *Gli1*^{Cre-ERT2}; *tdTomato*^{flx} and *Acta2-Cre-ERT2*; *tdTomato*^{flx} lungs was carried out using the Chromium Next GEM Single-Cell 3' Reagent Kit v3.1 (10x Genomics). After following the 10x Genomics library preparation protocol, all samples were sequenced on an Illumina NovaSeq 6000 sequencer. For demultiplexing and the subsequent FASTQ file generation we used Illumina's bcl2fastq (2.19.0.316). Sequencing reads were aligned to the mouse mm10 reference genome (refdata-gex-mm10-2020-A downloaded from 10xGenomics) using STAR solo (2.7.9a) resulting in three UMI count matrices for spliced, unspliced ambiguous counts per cell per gene in order to enable subsequent velocity analysis. During the alignment step UMI deduplication was performed by STAR. Droplet filtering was done using the EmptyDrops_CR parameter setting.

After quality control, resulting UMI count matrices from the raw output folder of the STAR solo results were pre-processed for further analyses using Scanpy (1.9.3) in a Python (3.9.12) environment.⁵⁷ To filter out low quality cells, doublets, cell debris or ambient

RNA the following filter criteria were applied to the data. We used scrublet with standard parameters to identify doublets. Cells were selected to contain a maximum of 15,000 and a minimum of 1,200 UMI counts. Less than 20% of all UMI counts are allowed to map to a mitochondrial origin. Finally, at least 600 different genes must be detectable (at least one read mapped to the gene) for each cell. To reduce the gene set size, only those genes were kept, which were expressed in at least 20 cells (function filter_cells with min_cells parameter set to 20). UMI counts underwent normalization in respect to the library size and such that each cell contains 10,000 reads using Scanpy's normalize_per_cell function. The resulting counts were log transformed using the log1p function. For dimensionality reduction and for data integration with Harmony PCAs were calculated. For that purpose 500 genes were selected as highly variable using the highly_variable_genes function. 20 principal components were identified using the pca function based on these highly variable genes. Harmony integration was performed using the harmony_integrate function using default parameters. A k-nearest-neighbor approach was applied to calculate a neighborhood graph using the neighbors function using default parameter setting (15 neighbors), on which Leiden clustering was performed with resolutions of 0.4, 0.6, 1.0 and 1.4. A two-dimensional visualization of the cells was achieved by calculating UMAPs. Next, automatic cell-type annotation was performed by calculating the average gene expression of all clusters individually. Data were compared to the Mouse Cell Atlas (MCA) using the scMCA R package (<https://github.com/ggjlab/scMCA>)⁵⁸ and later corrected by additional manual annotation according to LungMAP's CellCards classification (<https://lungmap.net/research/cell-cards/>). Differentially expressed genes (DEGs) were identified by the Scanpy rank_gene_groups function. The method parameter for the statistical testing procedure was selected as t test. For gene set enrichment analysis (GSEA) the genes were ranked for the negative decadic logarithm of the corresponding p-value multiplied by the sign of the log2-transformed fold change. GSEA was performed within R (version 4.3.1) using the GSEA function of the clusterProfiler (version 4.10) package⁵⁹ using default settings and a gene signature extracted from the scRNA-seq data by comparing the gene expression in p7 AMF versus all that of all other cells.

Velocity analysis was done using scVelo⁶⁰ using standard setting. The number of highly variable genes was set to 500. First and second order moments were calculated with the moments function with parameters n_pcs = 30 and n_neighbors = 30.

The data were exported in H5AD format and subsequently loaded into cellxgene v1.1.1 extended by the VIP plugin (v3.1). UMAP plots we generated with the *Embedding Plot* function of cellxgene. The gene specificity function was used to generate specificity heat maps indicating the ratio of the expression of a given gene in a specific cell type compared to the gene's expression across all cell types.

With cellxgene DEGs were calculated using the *DEG* function comparing selection of cells per cluster versus all other cells using Welch's t test in cellxgene. FDR significance was defined as > 0.05 with an absolute log2(Fold change) of 1. Gene enrichment and KEGG analysis were performed using ShinyGO (version 0.80).⁶¹ Mus musculus assembly with STRING-db ID mmusculus_gene_ensembl was used with mouse genes GRCm39 assembly (taxonomy ID 10090). Visualization was performed using GO Biological Process with FDR cutoff set at 0,05 and with 10 genes as minimum pathway requirement. Pathways were sorted by -log10(FDR) and colored with fold enrichment, and chart type was selected as either lollipop or barplot_inside. For the cell-cell interaction analysis, the single-cell atlas of mouse lung development⁴⁴ and the AMF & AMF-like cluster (Figure S7C) were integrated using Seurat (v4.3.0).⁶² The single-cell atlas of mouse lung development raw read counts (GSE165063) was extracted from the final processed data as were AMF & AMF-like raw read counts. Therefore, both datasets were only subjected to normalization with SCTransform prior to a dimensional reduction and followed by the integration using Seurat's Harmony algorithm implementation. Clustered data were annotated by label transfer from the pre-existing information. The cell-cell interaction analysis was performed using CellChat⁶³ (v2.1.1). Integrated data were subset for the time points "P7", "P28", "Mock" and "Tam-PR8" (Fig. S4). Each subset was analyzed individually with the CellChat pipeline as described in the vignette using standard parameters. CellChatDB.mouse was used as database. Circle plots were created using CellChat's netVisual_circle function. For the heatmap depicting ligand-receptor interaction between AMF/AMF-like cells and AT2 cells, probability values were first calculated by CellChat's netVisual_bubble and subsequently plotted with ComplexHeatmap (v2.6.2). The heatmap depicts the top 20 ligand-receptor interactions identified in P7 AMF to AT2 cells for all four time points. Gene specificity was calculated as the ratio between cumulative expression across all cells in a cluster (normalized to cell count) and the cumulative expression across all cells (also normalized).

Alveolosphere assay

FACS-sorted tdTom+ (mesenchymal) cells from *Gli1*^{Cre-ERT2}; *tdTomato*^{flox} lungs were centrifuged and then resuspended in Dulbecco's Modified Eagle Medium (Life Technologies). These cells were added to alveolar epithelial cells (AECs; defined as CD45^{neg} CD31^{neg} EpCAM^{low}) and mixed at a ratio of 1:1 with cold growth factor-reduced phenol red-free Matrigel (Corning). Cultures were maintained under air-liquid conditions at a temperature of 37°C with 5% CO₂ for a duration of 3 weeks to allow the formation of alveolar organoids (alveolospheres). The culture medium was changed every other day to provide optimal conditions for steady growth and development. Alveolospheres were imaged using EVOS M7000 (Thermo Fisher Scientific) and quantified using Fiji.

QUANTIFICATION AND STATISTICAL ANALYSIS

Quantitative data were assembled and analyzed using GraphPad Prism software (GraphPad Software). Results are presented as mean ± standard error of the mean (SEM). Statistical comparisons between two groups were performed using Student's t-test while one-way ANOVA was used for comparisons involving three or more groups with a single variable. Two-way ANOVA was employed for

comparisons involving multiple groups with two variables. Statistical significance was defined as $P < 0.05$. The number of biological replicates is indicated in the corresponding figure legends.

ADDITIONAL RESOURCES

All gene signatures and differentially expressed genes (DEGs) are provided in [Data S1](#).